Naval Ocean Research and Development Activity
August 1989 Report 240

Technical Description of the Optimum Thermal Interpolation System, Version 1: A Model for Oceanographic Data Assimilation

R. Michael Clancy
Ocean Models Division
Fleet Numerical Oceanography Center
Monterey, California 93943

Patricia A. Phoebus
Ocean Sensing and Prediction Division
Ocean Science Directorate

Kenneth D. Pollak
Ocean Models Division
Fleet Numerical Oceanography Center
Monterey, California 93943

Foreword

The Navy's Fleet Numerical Oceanography Center (FNOC) in Monterey, California, is responsible for providing three-dimensional global and regional scale analyses of ocean temperature to the Fleet. These products have a direct and important impact on the Navy's mission and daily operations. However, the amount of oceanographic data that exists is limited, at best, due to the vast ocean area that must be sampled and the relatively small number of ships and buoys available to make observations. While remotely sensed measurements are more abundant, large areas of the oceans are normally obscured by cloud cover. Furthermore, the only satellite data being directly used for temperature analysis at this time are the Multichannel Sea Surface Temperatures, which provide information only about the ocean's surface. Because of the data sparsity, especially below the surface, it is essential that we make optimum use of each observation.

The Naval Ocean Research and Development Activity has worked closely with scientists at FNOC to develop a new and improved thermal analysis product, the Optimum Thermal Interpolation System (OTIS), to meet this goal. This report describes in detail the state-of-the-art techniques that are employed in OTIS to produce a nowcast of the three-dimensional global ocean thermal structure. While OTIS is a useful environmental product in its own right, the output from OTIS provides the FNOC acoustic models with improved input data fields. Thus, the implementation of OTIS as FNOC's operational analysis has resulted in the delivery of superior environmental and acoustic products to the Fleet.

W B Moseley

W. B. Moseley
Technical Director

J B Tupaz

J. B. Tupaz, Captain, USN
Commanding Officer

Executive Summary

The Optimum Thermal Interpolation System (OTIS) is an ocean thermal analysis product developed for real-time operational use at the Fleet Numerical Oceanography Center. OTIS is expected to become the centerpiece of the Navy's ocean thermal analysis and prediction capabilities both ashore and afloat. It provides a rigorous framework for the synergistic combination of real-time data, climatology, and predictions from ocean mixed-layer and circulation models to produce the Navy's most accurate representation of ocean thermal structure on global and regional scales. OTIS is particularly well suited for utilization of remotely sensed data from satellites because of its ability to account for the relative accuracies of various types of data.

OTIS is based on the optimum interpolation (OI) data assimilation methodology. Basically, the OI technique maps observations distributed nonuniformly in space and time to a uniformly gridded synoptic representation, or analysis, of the target field. The analysis is constructed as a first-guess background field plus an anomaly relative to that field. The analyzed anomaly at a particular gridpoint is given by a weighted combination of observed and model-predicted anomalies, with the space-time autocorrelation function for the resolvable anomalies governing which observations contribute. The OI technique provides the optimum weights applied to each anomaly, such that the resulting analysis error will be minimized in a least-squares sense. The technique also provides an estimate of this error.

The basic inputs to OTIS are the statistics defining both the resolvable and subgrid-scale variability of the target field about the background field, the instrumental error characteristics of the measurement systems providing the observations, and the error characteristics of the forecast model that supplies the predictions. The end product is a statistically optimum gridded representation of the current ocean thermal structure, which may in turn be used to initialize prognostic thermodynamic and ocean circulation models, or to compute sound-speed profiles for input to ocean acoustic models.

Acknowledgments

We are happy to acknowledge the contributions made to OTIS by others. Dr. Paul May and Dr. Ted Bennett of NORDA's Ocean Hydrodynamics/ Thermodynamics Branch provided technical advice at various stages of the OTIS development, as did Mr. Jeff Hawkins of NORDA's Remote Sensing Branch. Ms. Bonnie Samuels, now at NOAA's Geophysical Fluid Dynamics Laboratory, played a key role in the early stages of OTIS implementation. Science Applications International Corporation, under contract with NORDA and FNOC, provided much of the programming support, through the efforts of Mr. George Innis, Mr. Bruce Mendenhall, and Ms. Mary Lou Morris. Later modifications were made by Mr. Harry Hamilton of ST Systems Corporation, also under contract to FNOC. All of their contributions were valuable.

This work was supported initially by the Naval Air Systems Command under Program Element 63207N, Automated Environmental Prediction System, Capt. J. Ford, Program Manager, and subsequently by the Space and Naval Warfare Systems Command under Program Elements 63207N, Air-Ocean Prediction, and Program Element 63704N, Satellite Applications and Technology, Capt. J. Jensen, Program Manager.

Contents

1.0 Introduction 1

2.0 Description of the Analysis Procedure 2
2.1 Sea Surface Temperature Analysis 2
2.2 Mixed-layer Analysis 5
2.3 Sub-mixed-layer Analysis 6

3.0 User-specified Parameters 6

4.0 Data Screening 7

5.0 Prediction Models 8
5.1 TOPS Model 8
5.2 Climatological Trend Model 9

6.0 Idealized Cases 9
6.1 Data-void Gridpoint 9
6.2 Isolated Observation at a Gridpoint 11
6.3 Two Observations Near a Gridpoint 13

7.0 Horizontal Analysis Grids 14

8.0 Supporting Climatologies 15

9.0 Ocean Feature Models 15

10.0 Example Output 15

11.0 Validation 15

12.0 Summary and Future Developments 20

13.0 References 23

Appendix: Basic Theory of Optimum Interpolation 27

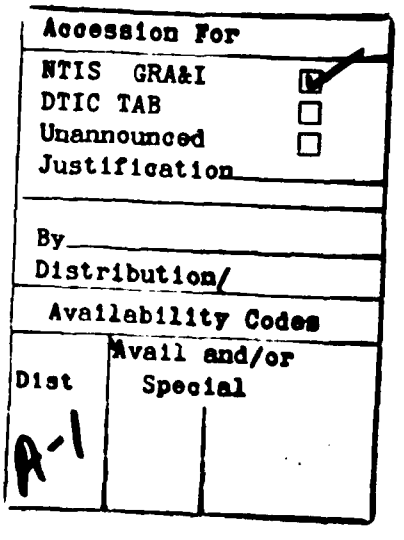

Definition of Symbols

B_o	Surface infrared radiative heat flux.
C_D	Atmospheric drag coefficient.
c	Specific heat of seawater.
d	Damping coefficient for inertial oscillations.
F	Downward flux of solar radiation.
F_o	Solar radiation penetrating the sea surface.
f	Coriolis parameter.
H_o	Surface sensible heat flux.
LQ_o	Surface latent heat flux.
S	Salinity.
S_o	Salinity at the sea surface.
T	Temperature.
T^R	Reference climatological SST gradient.
T_k^a	Analyzed temperature at gridpoint k.
T_k^c	Climatological temperature at gridpoint k.
T_i^o	Observed temperature at location i.
T_k^p	TOPS-predicted temperature at gridpoint k.
$(T_k^a)_{INITIAL}$	Temperature resulting from previous OTIS analysis.
τ_j	Individual MCSST observation at location j.
α_{ki}	Weight given to observation i assimilated at gridpoint k.
β_k	Weight given to TOPS prediction at gridpoint k.
γ_k	Weight given to climatology at gridpoint k.
$\varkappa$	Background eddy diffusion coefficient.
N	Number of observations assimilated at gridpoint k.
η_{ij}	Correlation between resolvable thermal anomalies at location i and location j in space-time.
λ_i^o	Noise-to-signal ratio for observation i.
λ_k^p	Noise-to-signal ratio for TOPS prediction at gridpoint k.
λ_i^n	Noise-to-signal ratio for subgrid-scale error at location i.
λ_{avg}^n	Average of λ_i^n over entire horizontal analysis domain.
Λ	Horizontal eddy diffusion coefficient.

ρ	Reference density for seawater.
ρ_a	Reference density for air near the surface.
A_k	Inverse of east-west decorrelation scale of resolvable thermal anomalies at gridpoint k.
B_k	Inverse of north-south decorrelation scale of resolvable thermal anomalies at gridpoint k.
C_k	Inverse of temporal decorrelation scale of resolvable thermal anomalies at gridpoint k.
D	Number of analysis cycles (days) for temperature anomaly to decay to 10% of initial value at a data void gridpoint.
U, V	x- and y-components of wind vector at height of 19.5 m above the sea surface.
u, v	x- and y-components of drift current.
u_g, v_g	x- and y-components of the geostrophic current.
u_a, v_a	x- and y-components of the advection current.
w_a	z-component of the advection current.
ΔX	Reference grid space.
Δx_{ij}	East-west distance between location i and location j.
Δy_{ij}	North-south distance between location i and location j.
Δt_{ij}	Time difference between observation i and observation j.
$(\Delta T_k^p)_n$	Change in TOPS predicted temperature from level n–1 to level n (level 0 implies the surface) at gridpoint k.
ΔT_{CLIM}	Climatological change in temperature between previous and current analysis times.
h_k^a	Analyzed mixed-layer depth at gridpoint k.
h_k^c	Climatological mixed-layer depth at gridpoint k.
h_i^o	Observed mixed-layer depth at gridpoint k.
σ_i^o	RMS observational error of observation i.
σ_k^p	RMS error of TOPS prediction at gridpoint k.
σ_i^c	Long-term RMS variation of resolvable thermal anomalies about climatology at location i.
σ_i^b	RMS difference between bathy observations and climatology at location i.

σ_{clim}^{b}	RMS difference between bathy observations and climatology calculated over entire horizontal analysis domain.
σ_k^c	Expected RMS temperature difference between T_k^a and independent bathy observations.
σ_i''	RMS subgrid scale error at location i.
σ_i'	RMS error added to MCSST super ob as a result of the way in which the block averaging of the MCSST data is done.
σ_k^a	RMS error of resolvable thermal field in resulting analysis at gridpoint k.
σ_k^∞	Steady-state value for σ_k^a at gridpoint which is devoid of data for a long period of time.
$(\sigma_i)_{EX}$	RMS error added to ith bathy observation below depth z_B by the downward extrapolation of the bathy.
ν_k	Anomaly reduction factor at gridpoint k.
M	Number of MCSST observations averaged around a gridpoint to form a "super ob."
ε	Standard deviation of instrumental error for MCSST, SHIP, and BATHY observations.
c	Mean of instrumental error (i.e., bias) for MCSST observations.
G_k	RMS TOPS error growth over one forecast cycle at gridpoint k.
z	Depth, measured positive downward from the surface in meters.
z_B	Deepest reported depth in a bathy observation.

Technical Description of the Optimum Thermal Interpolation System, Version 1: A Model for Oceanographic Data Assimilation

1.0 Introduction

The Optimum Thermal Interpolation System (OTIS) is an ocean thermal analysis product developed for real-time operational use at the Fleet Numerical Oceanography Center (FNOC). The development of OTIS Version 1 is described by Innis (1983), Innis (1985), Innis and Mendenhall (1986), and STX (1987); the OTIS 1 software is described by SAIC (1988a), SAIC (1988b), and SAIC (1988c).

OTIS is expected to become the centerpiece of the Navy's ocean thermal analysis and prediction capabilities both ashore and afloat. It provides a rigorous framework for the synergistic combination of real-time data, climatology, and predictions from ocean mixed-layer and circulation models to produce the Navy's most accurate representation of ocean thermal structure on global and regional scales. OTIS is particularly well suited for utilization of remotely sensed data from satellites. It can run on coarse-resolution grids with global coverage or on eddy-resolving grids with regional coverage. The OTIS 1 software, representing eight main programs and approximately 20,000 lines of source code, is well-documented and fully integrated into the FNOC computer system, and is under configuration management control. This report provides a complete and detailed technical description of OTIS 1 as it is now implemented at FNOC.

OTIS is based on the Optimum Interpolation (OI) data assimilation technique of Gandin (1965), which is used widely in meteorology. The OI technique has been applied to oceanographic analysis by Bretherton et al. (1976), Freeland and Gould (1976), McWilliams (1976), White (1977), Dorman and Saur (1978), White and Bernstein (1979), Bernstein and White (1981), Carter and Robinson (1981), Clancy (1983), Robinson (1983), Roemmich (1983), Robinson and Leslie (1985), McWilliams et al. (1986), Hua et al. (1986), Robinson (1986), Robinson and Walstad (1986), Robinson et al. (1986), Hansen and Herman (1986), Cummings (1986), Carter and Robinson (1987), Beasley (1987), Carton (1987), Murray (1987), Robinson et al. (1987), Carter et al. (1988), Grillaki-Steiert and Amoroso (1988), and others.

Basically, the OI technique maps observations distributed nonuniformly in space and time to a uniformly gridded synoptic representation, or analysis, of the target field. As in most objective analysis techniques, the concept of *resolvable* versus *subgrid-scale* features is fundamental in OI. Resolvable features are those of spatial extent greater than twice the mesh length of the analysis grid, and thus are capable of being at least marginally represented in discrete fashion by the grid. *Subgrid-scale* features are those with spatial extent less than twice the mesh length, which, as a result, cannot be resolved by the grid. As far as the analysis is concerned, subgrid-scale features contribute to the error in the observations.

An OI analysis is constructed as a background or "first-guess" field plus an anomaly relative to this field. The anomaly at a particular gridpoint is given by a weighted combination of observed and model-predicted anomalies, with the space-time autocorrelation function for the resolvable anomalies governing which observations contribute. The OI technique provides the optimum weights applied to the observations and predictions, such that the resulting analysis error will be minimized in a least-squares sense. The technique also provides an estimate of this error. The basic inputs to this process are the statistics defining both the resolvable and subgrid-scale variability of the target field about the background field, the instrumental error characteristics of the measurement systems providing the observations, and the error characteristics of the forecast model that supplies the predictions.

The remainder of this report is organized as follows. Section 2 gives a technically detailed description of the data assimilation technique used in OTIS. Section 3 discusses the user-specified free parameters required by the technique. Section 4 presents the data-screening algorithm used by OTIS to filter out spurious data. Section 5 provides a technical overview of the ocean prediction models used in conjunction with OTIS. Section 6 presents a series of idealized experiments that provide insight into how OTIS chooses the relative weighting of climatology, data, and model prediction to arrive at the analyzed temperature. Section 7 discusses the horizontal grids on which OTIS can

function and Section 8 discusses the climatologies it can use. Section 9 is a brief overview of the use of "ocean feature models," which allow OTIS to map the subsurface structure of fronts and eddies accurately from only their surface signatures. Section 10 shows examples of output generated by OTIS. Section 11 discusses the ongoing and automatic validation of OTIS against independent bathythermograph (hereafter referred to as "bathy") data at FNOC. Finally, Section 12 summarizes the central role OTIS plays in linking other data bases and models and discusses future developments.

Readers unconcerned with the technical details of OTIS should skip to Section 7.

2.0 Description of the Analysis Procedure

OTIS can be executed in either "shallow" or "deep" analysis modes. In the shallow mode, the deepest analyzed depth is 400 m, while in the deep mode it is 5000 m. In performing an analysis, OTIS proceeds point-by-point through its horizontal grid, producing a complete profile from the surface to the deepest analyzed depth at each gridpoint before advancing to the next. At each of these gridpoints, the analysis sequence is (1) sea surface temperature (SST), (2) temperature in the mixed layer, and (3) temperature below the mixed layer.

2.1 Sea Surface Temperature Analysis

OTIS follows the approach of Alaka and Elvander (1972) by using climatology as the first-guess field and treating input from a model prediction as a special type of observation. The model prediction is normally produced by the Thermodynamic Ocean Prediction System (TOPS) mixed-layer model described in Section 5. Thus, OTIS represents the analyzed SST at the kth gridpoint T_k^a as

$$T_k^a = T_k^c + \sum_{i=1}^{N} \alpha_{ki}(T_i^o - T_i^c) + \beta_k(T_k^p - T_k^c), \tag{2-1}$$

where T_k^c is the climatological temperature at the gridpoint valid at analysis time, T_k^p the predicted temperature at the gridpoint produced by a 24-hour TOPS forecast from the previous day's OTIS analysis, T_i^o the observed temperature at location i, T_i^c the climatological temperature at location i valid at the time of observation i, α_{ki} the weight applied to the ith observed climatological anomaly assimilated at the gridpoint, β_k the weight applied to the TOPS-predicted anomaly at the gridpoint, and N the number of observations assimilated at the gridpoint.

From the basic theory of OI (e.g., see Alaka and Elvander, 1972, or the Appendix of this report), the weights α_{ki} and β_k necessary to produce a statistically optimum analysis (i.e., one that will have a minimal mean-square error when averaged over a large number of analysis realizations) are obtained by solving the following set of $N+1$ equations

$$\eta_{ki} = \sum_{j=1}^{N} (\eta_{ij} + \delta_{ij}\lambda_i^o)\alpha_{kj} + (\eta_{ik} + \delta_{ik}\lambda_k^p)\beta_k \tag{2-2}$$

$$\text{for } i = 1,2,\ldots N,(N+1) = k,$$

where η_{ij} is the space-time autocorrelation between climatological anomalies at location i and location j ("location k" implies the gridpoint), λ_i^o is the noise-to-signal ratio for the ith observation, λ_k^p is the noise-to-signal ratio for the TOPS prediction, and δ_{ij} is the Kronecker delta function defined as

$$\delta_{ij} = 1 \quad \text{for } i = j$$

$$\delta_{ij} = 0 \quad \text{for } i \neq j.$$

The autocorrelation function η_{ij} is taken to be

$$\eta_{ij} = \exp(-A_k^2\Delta x_{ij}^2 - B_k^2\Delta y_{ij}^2 - C_k^2\Delta t_{ij}^2) \tag{2-3}$$

where Δx_{ij}, Δy_{ij} and Δt_{ij} are the east-west, north-south, and time separations between locations i and j in space-time; A_k, B_k and C_k are the inverses of the east-west, north-south and time decorrelation scales; and location k implies the gridpoint at analysis time. This functional form for η has been used widely in meteorological and oceanographic analysis. The quantities A, B and C are user-specified parameters that must be chosen to reflect the ocean's resolvable variability about climatology. They tend to control the space-time domain over which an individual observation will influence the analysis.

The quantities λ_i^o and λ_k^p in equation (2-2) are given by

$$\lambda_i^o = \left[\frac{\sigma_i^o}{\sigma_i^c}\right]^2 \tag{2-4}$$

and

$$\lambda_k^p = \left[\frac{\sigma_k^p}{\sigma_k^c}\right]^2, \tag{2-5}$$

where σ_i^o is the root-mean-square (RMS) error of the ith observation, σ_k^p is the RMS error of the TOPS prediction at gridpoint k, and σ_i^c and σ_k^c are the RMS variations of the thermal field about climatology at location i and gridpoint k, respectively.

Determination of σ_i^o for use in equation (2-4) depends primarily on what type of data the *i*th observation is. Three types of data contribute to the OTIS SST analysis: ship injection/bucket temperature measurements, bathythermograph measurements, and Multi-Channel Sea Surface Temperature (MCSST) measurements from the Advanced Very High Resolution Radiometer (AVHRR) instrument aboard the National Oceanic and Atmospheric Administration's polar-orbiting satellites. For ship and bathy measurements, σ_i^o is given by

$$(\sigma_i^o)^2_{SHIP} = \varepsilon^2_{SHIP} + (\sigma_i^n)^2 \tag{2-6}$$

and

$$(\sigma_i^o)^2_{BATHY} = \varepsilon^2_{BATHY} + (\sigma_i^n)^2 \tag{2-7}$$

where ε_{SHIP} is the standard deviation of the instrumental error for the ship SST measurements, ε_{BATHY} is the standard deviation of the instrumental error for the bathy measurements, and σ_i^n is the RMS subgrid-scale error at location *i* (i.e., the RMS value of thermal anomalies with spatial extent less than twice the mesh length of the analysis grid and thus unresolvable by the grid). The quantities ε_{SHIP} and ε_{BATHY} are user-specified parameters that include the effect of basic instrumental error, as well as report and transmit errors. Note that the ship and bathy errors are assumed to have negligible means, so that ε_{SHIP} and ε_{BATHY} can also be thought of as the RMS errors. The values of ε_{SHIP} and ε_{BATHY} are chosen to reflect the general reliability of these data and tend to control their weighting relative to climatology, other data, and TOPS in the analysis.

The MCSST data are handled in a special way, which complicates the determination of $(\sigma_i^o)^2_{MCSST}$. Before assimilation into the analysis, the MCSST reports within one-half mesh length of each gridpoint are block averaged around the gridpoint to form "super obs" assumed valid at the gridpoint. This averaging process is done because the high MCSST data densities usually result in many MCSST reports around a gridpoint, and this process provides an efficient way to incorporate these data without losing any information on the *resolvable* thermal field. Thus, if the *i*th observation in equation (2-1) is an MCSST observation, then it is in fact given by

$$(T_i^o)_{MCSST} = \frac{1}{M}\sum_{j=1}^{M} \tau_j , \tag{2-8}$$

where τ_j is the *j*th individual MCSST report and M is the total number of individual MCSST reports used in the block average. Thus, in view of equation (2-8), the expression for $(\sigma_i^o)^2_{MCSST}$ becomes

$$(\sigma_i^o)^2_{MCSST} = \frac{1}{M}[\varepsilon^2_{MCSST} + (\sigma_i^n)^2 + (\sigma_i^r)^2] + e^2_{MCSST} , \tag{2-9}$$

where ε_{MCSST} and e_{MCSST} are the standard deviation and mean, respectively, of the instrumental error for the MCSST reports, and σ_i^r is the standard deviation of the SST field resulting from resolvable SST variations over the domain in which the MCSST block averaging is done. The term $(\sigma_i^r)^2$ represents the variance added because the differencing of the MCSST data with climatology is done *after* the block averaging and with the climatological temperature valid at the gridpoint, rather than *before* the block averaging and with temperatures obtained by interpolating climatology to each individual MCSST observation. This term is estimated by assuming a constant reference SST gradient and averaging the resulting temperature variance over one grid space. Thus,

$$(\sigma_i^r)^2 = \frac{(T^g \Delta X)^2}{12} \tag{2-10}$$

where T^g is a reference climatological SST gradient (taken to be 0.01°C km^{-1}) and ΔX is a reference grid space for the OTIS grid. Thus, for the FNOC 63 × 63 hemispheric grid (ΔX = *320 km*), σ_i^r = 0.85°C.

No attempt is made to correct for any mean error (i.e., bias) in the MCSST data. Rather, e^2_{MCSST} effectively becomes a lower bound on the MCSST observational error when M becomes large. The quantities ε_{MCSST} and e_{MCSST} are user-specified parameters that tend to control the relative weighting of the MCSST data in the analysis.

The individual MCSST reports that contribute to the super obs have varying ages, extending up to the length of time defining the temporal window for this type of data (see Section 4). The age assigned to the resulting super obs, however, is set to 48 hours relative to the analysis date-time group.

The value of σ_k^p for use in equation (2-5) is obtained from

$$(\sigma_k^p)^2 = (\sigma_k^a)^2_{INITIAL} + G_k^2 , \tag{2-11}$$

where $(\sigma_k^a)_{INITIAL}$ is the RMS error of the resolvable thermal field from the previous analysis initializing TOPS, and G_k is the RMS TOPS error growth over

one analysis-forecast-analysis cycle (i.e., 24 hours). Thus, following the approach of Bengtsson and Gustafsson (1972), the error in the predicted thermal field is taken to be the error in the initial conditions plus the error added due to error growth in the forecast model. The quantity G is a user-specified parameter that must be chosen to reflect the rate of error growth in TOPS. It tends to control the weight assigned to TOPS relative to climatology and data.

The last user-specified parameter used in OTIS is the noise-to-signal ratio for the subgrid scale error λ_i^n defined by

$$\lambda_i^n = \left[\frac{\sigma_i^n}{\sigma_i^c}\right]^2 . \tag{2-12}$$

Like A, B, and C, this quantity must be chosen to reflect the statistics of ocean thermal variability. For example, λ_i^n must be chosen larger in dynamically active regions, where subgrid-scale eddies produce large-amplitude but unresolved perturbations in the thermal field, than in more quiescent regions where the eddy field is weak. Of course, λ_i^n is a function of the grid mesh length, becoming smaller as the grid becomes finer and the unresolved portion of the thermal field decreases.

Equation (2-12) is used along with the RMS difference between bathy-observed temperatures and climatology σ_i^b to obtain σ_i^c and σ_i^n. Neglecting ε_{BATHY}, which is small compared to σ_i^n for the grids currently utilized by OTIS, $(\sigma_i^b)^2$ becomes

$$(\sigma_i^b)^2 = (\sigma_i^c)^2 + (\sigma_i^n)^2 \tag{2-13}$$

or just the sum of the mean-square resolvable signal about climatology plus the mean-square subgrid-scale noise. From (2-12) and (2-13),

$$(\sigma_i^c)^2 = \frac{(\sigma_i^b)^2}{1 + \lambda_i^n} \tag{2-14}$$

$$(\sigma_i^n)^2 = \frac{\lambda_i^n}{1 + \lambda_i^n} (\sigma_i^b)^2 . \tag{2-15}$$

For practical considerations (e.g., bathy data coverage), it is not possible to calculate $(\sigma_i^b)^2$ directly from bathy data at every observational location. Therefore, $(\sigma_i^b)^2$ is estimated from

$$(\sigma_i^b)^2 = \frac{1 + \lambda_i^n}{1 + \lambda_{av}^n} (\sigma_{av}^b)^2 , \tag{2-16}$$

where $(\sigma_{av}^b)^2$ is the mean-square departure of the bathy observations from climatology and λ_{av}^n is the average value of λ_i^n, both calculated over the entire analysis domain. The data used in this calculation consist of a running 60-day window of bathy observations reported to FNOC in real time, amounting to about 9000 reports.

Using the assumption of equation (2-16), equations (2-14) and (2-15) become

$$(\sigma_i^c)^2 = \frac{(\sigma_{av}^b)^2}{1 + \lambda_{av}^n} \tag{2-17}$$

$$(\sigma_i^n)^2 = \frac{\lambda_i^n}{1 + \lambda_{av}^n} (\sigma_{av}^b)^2 . \tag{2-18}$$

With λ_i^n specified by the user, and σ_{av}^b and λ_{av}^n calculated internally by OTIS, equations (2-17) and (2-18) provide σ_i^c and σ_i^n for use in equations (2-4), (2-5), (2-6), (2-9), and (2-12). Note that σ_{av}^b, and thus σ_i^c and σ_i^n, are determined separately for each standard level of the OTIS vertical output grid (see Section 2.2).

Note also from equation (2-17) that σ_i^c is independent of horizontal location. Thus, implicit in equation (2-16) is the assumption that variations of σ_i^b with location are produced entirely by variations in σ_i^n.

Equations (2-2) through (2-12) and (2-17) through (2-18) constitute a closed set, which can be solved for the weights α_{ki} and β_k. Once these weights are obtained, the analyzed temperature is calculated from equation (2-1). Also, from the basic theory of OI (see for example White and Bernstein, 1979), the RMS error of the resolvable thermal field σ_k^a can then be calculated from

$$(\sigma_k^a)^2 = (\sigma_k^c)^2 \left(1 - \beta_k - \sum_{i=1}^{N} \alpha_{ki} \eta_{ki}\right) . \tag{2-19}$$

Recognizing that OTIS initializes the TOPS forecast, which will provide T_k^p for the following day's analysis, the value of $(\sigma_k^a)^2$ obtained from (2-19) becomes $(\sigma_k^a)^2_{INITIAL}$ of equation (2-11) (i.e., the error in the TOPS initial conditions) for the following day's analysis.

Finally, the expected departure of the thermal field from an independent bathy observation made precisely at the gridpoint at analysis time σ_k^e is given by

$$\sigma_k^e = \left[(\sigma_k^a)^2 + (\sigma_k^n)^2 + \varepsilon^2_{BATHY}\right]^{0.5} . \tag{2-20}$$

The three terms inside the brackets represent the contributions of analysis error, subgrid-scale error, and instrumental error. For a large set of such comparisons, approximately 68% of the independent bathy observations would differ from the analyzed temperature T_k^a by less than σ_k^e, and approximately 96% would differ by less than $2\sigma_k^e$. In such dynamically active regions as the Gulf Stream or the Kuroshio, σ_k^n and, hence, σ_k^e will be large compared to values in more quiescent regions, such as the eastern Pacific.

2.2 Mixed-layer Analysis

Upon conclusion of the SST analysis at gridpoint k, OTIS performs an OI analysis for mixed-layer depth (MLD). In analogy to equation (2-1), the expression for the analyzed MLD h_k^a is

$$h_k^a = h_k^c + \sum_{i=1}^{N} \alpha_{ki}(h_i^o - h_i^c) + \beta_k(h_k^p - h_k^c), \quad (2\text{-}21)$$

where h_k^c is the climatological MLD at the gridpoint, h_k^p the predicted MLD at the gridpoint from the 24-hour TOPS forecast from the previous day's analysis, h_i^o the observed MLD at location i, h_i^c the climatological MLD at location i, α_{ki} the weight applied to the ith observed climatological MLD anomaly assimilated at the gridpoint, β_k the weight applied to the TOPS-predicted MLD anomaly at the gridpoint, and N the number of observations assimilated at the gridpoint.

The climatological MLD h_k^c is determined from examination of the climatological temperature profile, defined at gridpoint k on the vertical grid of Table 2-1. Beginning at the surface and working downward, vertical temperature gradients are examined to find the shallowest pair of gridpoints between which the vertical gradient is less than $-0.05°C\ m^{-1}$. The layer depth h_k^c is then taken simply as the depth of the shallower gridpoint of this pair, and is thus always one of the discrete levels listed in Table 2-1. Exactly the same process is carried out on the TOPS and bathy profiles to define h_k^p and h_i^o. The TOPS profile is also defined on the upper 15 levels of Table 2-1, but the depths defining the bathy profiles are arbitrary; thus, h_i^o generally falls somewhere in between the fixed levels of Table 2-1.

The weights α_{ki} and β_k in equation (2-21) are obtained by solving the $N + 1$ equations of (2-2), as before. In solving (2-2), the parameters η_{ij}, λ_i^o, and λ_k^p are assumed equal to the corresponding values for temperature analysis at the 100-m depth. This assumption implies

$$(\sigma_i^o)_{\mathrm{MLD}} = (K)(\sigma_i^o)_{100\ \mathrm{m}}, \quad (2\text{-}22)$$

$$(\sigma_k^p)_{\mathrm{MLD}} = (K)(\sigma_k^p)_{100\ \mathrm{m}}, \quad (2\text{-}23)$$

and

$$(\sigma_k^c)_{\mathrm{MLD}} = (K)(\sigma_k^c)_{100\ \mathrm{m}}, \quad (2\text{-}24)$$

where the subscript "MLD" indicates values are for MLD variations, and K is a constant.

Although h_k^c and h_k^p can only take on the discrete values of Table 2-1, h_k^a resulting from the solution of (2-21) and (2-2) can take on any value. Thus, it can be thought of as a "floating level" in the analysis system.

With the analysis for h_k^a complete, OTIS sets the temperatures at the gridpoints of Table 2-1 that are shallower than h_k^a according to

$$(T_k^a)_m = (T_k^a)_0 + \sum_{n=1}^{m} (\Delta T_k^p)_n, \quad (2\text{-}25)$$

Table 2-1. Vertical grid for OTIS output.

LEVEL	DEPTH IN METERS
1	2.5
2	7.5
3	12.5
4	17.5
5	25.0
6	32.5
7	40.0
8	50.0
9	62.5
10	75.0
11	100.0
12	125.0
13	150.0
14	200.0
15	300.0
16	400.0
17	500.0
18	600.0
19	700.0
20	800.0
21	900.0
22	1000.0
23	1100.0
24	1200.0
25	1300.0
26	1400.0
27	1500.0
28	1750.0
29	2000.0
30	2500.0
31	3000.0
32	4000.0
33	5000.0

where $(T_k^a)_m$ is the analyzed temperature at level m, $(T_k^a)_0$ is the analyzed SST, and $(\Delta T_k^p)_n$ is the change in TOPS-predicted temperature from level $n-1$ to level n (level 0 implies the surface). Thus, the *shape* of the temperature profile from the surface to the base of the mixed layer (e.g., isothermal, weakly stratified, or multiple thermocline) is controlled exactly by TOPS.

2.3 Sub-mixed-layer Analysis

After the mixed-layer analysis at gridpoint k is complete, OTIS performs an analysis for the temperature profile below the analyzed MLD. Below this level, OTIS utilizes a completely variable or "floating" grid system designed to concentrate resolution in regions of high vertical gradient. Beginning at the MLD and working downward, the mesh spacing of this floating grid Δz is defined as

$$\Delta z = 50\,\mathrm{m} + (400\,\mathrm{m}^2\,C^{-1})\frac{\partial T_k^p}{\partial z} - (10\,\mathrm{m}^3\,C^{-2})\frac{\partial^2 T_k^p}{\partial z^2} \qquad (2\text{-}26)$$

$$\text{for } 5\,\mathrm{m} \le \Delta z \le 80\,\mathrm{m},$$

with z taken positive downward from the sea surface.

With the vertical grid extending from the base of the mixed layer downward to 400 m, defined by (2-26), OTIS performs an analysis for temperature at each of these levels. This analysis is carried out by solving (2-1) and (2-2) at each of the floating levels. If the deep analysis mode is selected, OTIS also carries out the same analysis at the fixed levels 17-33 of Table 2-1.

In general, the bathy observations which contribute to the sub-mixed-layer analysis extend to varying depths. Bathy observations that reach to less than 250 m, or which have $\frac{\partial}{\partial z}\left|(T_i^o - T_i^c)\right| > 0.01\,^\circ\mathrm{C\,m^{-1}}$ near their deepest reported depth z_B, are used in the analysis only for levels above z_B. Observations extending to greater than 250 m depth for which $\frac{\partial}{\partial z}\left|(T_i^o - T_i^c)\right| \le 0.01\,^\circ\mathrm{C\,m^{-1}}$ near z_B are used in the analysis at all levels down to 400 m, however, by extrapolating $(T_i^o - T_i^c)$ downward. The mean-square error added to the "observation" below z_B by this extrapolation is estimated from

$$(\sigma_i'')^2_{EX} = \left(0.0225 + 0.02\exp\{-0.05\,(z_B - 250)\}\right)(z - z_B), \qquad (2\text{-}27)$$

where z is the depth of the extrapolation point for the ith bathy in meters. Equation (2-7) for extrapolated bathy observations below z_B then becomes

$$(\sigma_i'')^2_{BATHY} = \varepsilon^2_{BATHY} + (\sigma_i'')^2 + (\sigma_i'')^2_{EX}. \qquad (2\text{-}28)$$

The quantities η_{ij}, λ_i'', and λ_i'' required in (2-2) are derived from the user-specified parameters A_k, B_k, C_k, λ_i^n and ε_{BATHY} as before. In calculating λ_i'' and λ_k'' via (2-4), (2-5), and (2-7), the quantities σ_i^c, σ_i^n and σ_i'' are vertically interpolated from the fixed-levels of Table 2-1 to the floating levels. Equation (2-28) is used in place of (2-7) for extrapolated bathy observations below z_B as discussed above. Note that the parameters A_k, B_k, C_k, and λ_i^n for sub-mixed-layer analysis can be assigned values by the user distinctly different from those at the surface. This is particularly important for C_k, which generally has a much smaller value below the MLD reflecting the much longer time-scale variability there.

Upon conclusion of the sub-mixed-layer temperature analysis, the analyzed temperatures at the floating levels defined by (2-26) are vertically interpolated to the fixed levels of Table 2-1 between the MLD and the 400-m depth for output. Thus, the final OTIS surface-to-400 m (shallow mode) or surface-to-5000 m (deep mode) temperature profile is defined at the levels of Table 2-1. The upper 15 levels of this grid are shared with TOPS, while the lower 18 are shared with the GDEM ocean thermal climatology (see Section 8).

As a final output step for the deep analysis mode, the analyzed vertical temperature profile below 400 m is altered where necessary to blend with the vertical temperature profile analyzed above using the Navy-standard merge algorithm. This step is necessary because 400 m represents a discontinuity in data density, corresponding to the nominal depth of most bathy observations.

3.0 User-specified Parameters

The nine user-specifed parameters used in OTIS are listed in Table 3-1.

Table 3-1. User-specified parameters.

PARAMETER	VALUE
ε_{SHIP}	2.29°C
ε_{BATHY}	0.20°C
ε_{MCSST}	0.71°C
e_{MCSST}	0.22°C
C	1/(20 days) above the MLD. 1/(60 days) below the MLD.
A	Variable, defined in latitude/longitude bands, separate values for above and below the MLD.
B	" " "
G	" " "
λ^n	" " "

The values of ε_{SHIP} and ε_{BATHY} are obtained from Earle (1985) and from White and Bernstein (1979), respectively. The values of ε_{MCSST} and e_{MCSST} are based on Hawkins et al. (1986) and Strong and McClain (1985). The values of A and B range from 1/(2500 km) in low-latitude open-ocean regions to 1/(100 km) in coastal regions. The values of G and λ^n vary widely. In general, G is smaller in midlatitude open-ocean regions than in tropical or western-boundary current regions, where the atmospheric forcing and/or physics of TOPS is not fully adequate. In general, λ^n is smaller in quiescent regions (e.g., eastern Pacific) than in dynamically active regions characterized by strong mesoscale eddies which are unresolved by the horizontal grid (e.g., Kuroshio or Gulf Stream regions).

4.0 Data Screening

OTIS utilizes only data that fall within certain temporal and spatial windows (see Phoebus, 1988). For the SST analysis, the temporal window includes all data 0 to 60 hours prior to the OTIS run time. For the MLD and sub-mixed-layer analyses, the window includes all bathys from 0 to 60 days prior to the OTIS run time.

The spatial window is defined as ± 1 correlation scale in the north-south and east-west directions about the gridpoint. Before data are selected from this window, however, the bathy data are screened by applying a sorting process that limits the bathy data density in $2.5° \times 2.5°$ latitude/longitude squares to the 60 most recent reports, with no more than 30 taken from the same platform. This thinning process is a practical necessity for handling ocean weather stations, which typically report two bathy observations per day.

In addition, OTIS applies a ship-tracking algorithm, patterned after the approach of Mendenhall and Cuming (1980), to screen out bathy reports with obvious position errors. These types of errors are fairly common in the real-time bathy data set and result primarily from coding and radio transmission errors (e.g., latitude and longitude transposed, wrong hemisphere, etc.). Thus, OTIS monitors the successive positions of each ship reporting bathy observations at any time during the previous 60-day period and flags movements that reflect impossibly large ship speeds. Bathy observations corresponding to the erroneous position reports are excluded from further processing by OTIS.

For the SST analysis, up to 700 reports within the spatial window are collected without regard to relative correlation or data type (i.e., ship, bathy, MCSST). Data in excess of the 700-report limit are ignored, but this rarely happens in practice. These data are then sorted to select the 15 reports most highly correlated with the gridpoint, again without regard to data type.

The 15 most highly correlated reports are then screened for spurious data using the "buddy check" approach of Phoebus (1989), which is patterned after that of Dimego et al. (1985). Hence, the inequality

$$\left|(T_i^o - T_i^c) - (T_j^o - T_j^c)\right| \leq (3 - 1.5\,\eta_{ij})\sigma^c \qquad (4\text{-}1)$$

is examined. If the inequality is satisfied, then observations i and j corroborate each other and are thus both given "keep flags" equal to the correlation between them, η_{ij}; if the inequality is not satisfied, then the observations contradict each other and are thus both given "toss flags" equal to η_{ij}. Following examination of all remaining pairs of reports, the single observation with the highest summation of toss flags is removed if the summation exceeds 2. Observations whose keep flags sum to more than 2 are retained regardless of toss flag settings. This process, beginning with the examination of the inequality (4-1), is then repeated until no observations have toss flags that sum to more than 2. The remaining observations are utilized in the SST analysis at the gridpoint.

Screening of the bathy data used in the MLD and sub-mixed-layer analyses proceeds in similar fashion. Up to 700 bathy reports are selected in the spatial window without regard to their relative correlation with the gridpoint. The data are then sorted to retain only the 15 observations most highly correlated with the gridpoint. Finally, the buddy check of equation (4-1) is applied to the 15 most highly correlated observations to eliminate spurious reports.

OTIS also compiles a list of bathy reports rejected via the buddy check described above. This list can be sorted in various ways and output daily or weekly as an aid to analysts performing subjective bathy error correction via the Quality Improvement Profile System (QUIPS) at FNOC (see McLain et al., 1986).

OTIS also includes the capability to exclude individual bathy reports identified by quality control personnel as being suspect, *even* if they pass the internal OTIS data screening checks. Information identifying these reports is simply typed into a disk file, which OTIS automatically checks each run. This process allows convenient application of an additional level of data quality control.

Finally, an additional data screening capability can be used in certain regional applications of OTIS. An option exists to decorrelate data from the analysis across fronts and eddy boundaries, which are determined from an analyst's interpretation of satellite imagery and represented on the FNOC data base in message format. If this option is selected, then OTIS will read the front and eddy messages from the FNOC data base, determine the location of fronts and eddy boundaries, and truncate the spatial windows used for

data selection around each gridpoint to ensure that data on one side of a front or eddy boundary does not contribute to the analysis at gridpoints on the other side of the front or eddy boundary. Thus, in effect, a water-mass-based analysis is achieved with observations made in a particular water mass (e.g., shelf water, slope water, Gulf Stream water, Sargasso Sea water, warm-core ring, cold-core ring, etc.) affecting only gridpoints contained within that water mass.

5.0 Prediction Models

The predicted temperature T_k^p required by OTIS is normally taken from a 24-hour forecast produced by the TOPS mixed-layer model (see Clancy and Martin, 1981; Clancy and Pollak, 1983; Martin et al., 1985) initialized from the previous day's OTIS analysis. Thus, OTIS and TOPS are coupled in an analysis-forecast-analysis data assimilation cycle. OTIS also, however, includes the capability to use a "climatological trend" model in place of TOPS as described below.

5.1 TOPS Model

The aim of TOPS is to forecast the response of the mixed layer and mid-ocean fronts to atmospheric forcing. The prognostic equations for TOPS express conservation of temperature, salinity, and momentum in the upper ocean as follows:

$$\frac{\partial T}{\partial t} = \frac{\partial}{\partial z}\left(-\overline{w'T'} + \varkappa\frac{\partial T}{\partial z}\right) + \frac{1}{\rho c}\frac{\partial F}{\partial z} - \frac{\partial}{\partial x}(u_a T) - \frac{\partial}{\partial y}(v_a T) - \frac{\partial}{\partial z}(w_a T) + \Lambda\left(\frac{\partial^2 T}{\partial x^2} + \frac{\partial^2 T}{\partial y^2}\right) \tag{5-1}$$

$$\frac{\partial S}{\partial t} = \frac{\partial}{\partial z}\left(-\overline{w'S'} + \varkappa\frac{\partial S}{\partial z}\right) - \frac{\partial}{\partial x}(u_a S) - \frac{\partial}{\partial y}(v_a S) - \frac{\partial}{\partial z}(w_a S) + \Lambda\left(\frac{\partial^2 S}{\partial x^2} + \frac{\partial^2 S}{\partial y^2}\right) \tag{5-2}$$

$$\frac{\partial u}{\partial t} = fv + \frac{\partial}{\partial z}\left(-\overline{w'u'} + \varkappa\frac{\partial u}{\partial z}\right) - du \tag{5-3}$$

$$\frac{\partial v}{\partial t} = -fu + \frac{\partial}{\partial z}\left(-\overline{w'v'} + \varkappa\frac{\partial v}{\partial z}\right) - dv \tag{5-4}$$

where T is the temperature, S the salinity, u and v the x- and y-components of the current velocity (x and y horizontal coordinates defined relative to the TOPS grid), w the z-component of the current velocity, F the downward flux of solar radiation, ρ a reference density, c the specific heat of seawater, d a damping coefficient, $\varkappa$ a diffusion coefficient, f the Coriolis parameter, Λ the horizontal eddy diffusion coefficient, t the time, z the vertical coordinate (positive upward from the sea surface), and u_a, v_a, w_a the x-, y-, and z-components of an advection current defined below.

The terms involving d in (5-3) and (5-4) represent the drag force caused by the radiation stress at the base of the mixed layer associated with the propagation of internal wave energy downward and away from the wind-forced region (see Pollard and Millard, 1970). The terms involving $\varkappa$ account for very weak "background" eddy diffusion (due to intermittent breaking of internal waves, for example) that exists even below the mixed layer. The terms involving Λ represent horizontal eddy diffusion patterned after that of Haney (1974).

The terms $\overline{w'T'}$, $\overline{w'S'}$, $\overline{w'u'}$, and $\overline{w'v'}$ represent the vertical eddy (i.e., turbulent) fluxes of temperature, salinity, and momentum. These terms account for the major portion of the mixed-layer's response to atmospheric forcing and are parameterized with the Level-2 turbulence closure theory of Mellor and Yamada (1974) and Mellor and Durbin (1975). The upper boundary conditions for these terms constitute the surface fluxes of heat, moisture, and momentum, which drive the TOPS forecasts. Thus,

$$\left[-\overline{w'T'} + \varkappa\frac{\partial T}{\partial z}\right]_{z=0} = \frac{-(B_o + H_o + LQ_o)}{\rho c}, \tag{5-5}$$

$$F_{z=0} = F_o \tag{5-6}$$

$$\left[-\overline{w'S'} + \varkappa\frac{\partial S}{\partial z}\right]_{z=0} = \frac{Q_o S_o}{\rho}, \tag{5-7}$$

$$\left[-\overline{w'u'} + \varkappa\frac{\partial u}{\partial z}\right]_{z=0} = \frac{\rho_a C_D U(U^2 + V^2)^{0.5}}{\rho}, \tag{5-8}$$

and

$$\left[-\overline{w'v'} + \varkappa\frac{\partial v}{\partial z}\right]_{z=0} = \frac{\rho_a C_D V(U^2 + V^2)^{0.5}}{\rho}, \tag{5-9}$$

where B_o is the surface infrared radiative heat flux, H_o is the surface sensible heat flux, LQ_o is the surface latent heat flux, F_o is the surface solar heat flux, S_o is the surface salinity, ρ_a is the density of the air near the surface, C_D is a drag coefficient, and U and V are the components of the wind velocity vector at a reference height of 19.5 m above the sea surface. The quantities B_o, H_o, LQ_o, F_o, U, and V are provided by either the Navy Operational Global Atmospheric Prediction System (NOGAPS; see Rosmond, 1981) or the Navy Operational Regional Atmospheric Prediction System (NORAPS; see Hodur, 1982) models, depending on the scale and area of application.

Because there are no horizontal pressure gradient terms in (5-3) and (5-4), u and v represent the wind-drift (i.e., Ekman plus inertial) component of the current. Neglect of horizontal pressure gradients here is motivated by the fact that geostrophic currents generally do not play an important role in mixed-layer dynamics. Still, TOPS allows geostrophic currents supplied from an external source to contribute to the advection. Thus,

$$u_a = u + u_g , \tag{5-10}$$

$$v_a = v + v_g , \tag{5-11}$$

and

$$w_a = \int_z^0 \left(\frac{\partial}{\partial x} u_a + \frac{\partial}{\partial y} v_a\right) dz , \tag{5-12}$$

where u_g and v_g are the x- and y-components of the geostrophic current. The source of these geostrophic currents will ultimately become eddy-resolving dynamical ocean circulation models (collectively identified by the acronym OCEANS) that will run independently of TOPS (see Hurlburt, 1984). This input will allow a much improved representation of the thermal field associated with fronts and eddies, even in the absence of in situ data. Even without geostrophic advection currents, however, TOPS contains the essential physics necessary to predict much of the evolution of the subarctic and subtropical fronts (Roden, 1977; Roden and Paskausky, 1978).

See Clancy and Pollak (1983) and FNOC (1986) for a detailed and complete discussion of TOPS and its implementation at FNOC.

5.2. Climatological Trend Model

OTIS has the capability to utilize a "climatological trend" model in lieu of TOPS to provide T_k^p at any or all of the OTIS analysis levels listed in Table 2-1. In this case,

$$T_k^p = (T_k^a)_{INITIAL} + \Delta T_{CLIM} \tag{5-13}$$

where $(T_k^a)_{INITIAL}$ is the temperature at the appropriate level resulting from the previous OTIS analysis (typically 24 hours earlier) and ΔT_{CLIM} is the *climatological* change in temperature at this level between the time of the previous analysis and the current analysis time. As is the case for TOPS, the error growth rate G_k is specified in latitude-longitude rectangles by the user.

This option provides the flexibility to run OTIS in regions for which there is no TOPS model available.

6.0 Idealized Cases

In this section we present idealized cases that illustrate certain aspects of the OI analysis technique as implemented in OTIS.

6.1 Data-void Gridpoint

In the case of a data-void gridpoint, equation (1) reduces to

$$T_k^a = T_k^c + \beta_k (T_k^p - T_k^c) , \tag{6-1}$$

which can be written

$$T_k^a = T_k^p - \nu_k (T_k^p - T_k^c) , \tag{6-2}$$

where

$$\nu_k = 1 - \beta_k . \tag{6-3}$$

The second term on the right side of (6-2) is an "anomaly decay term," which attempts to return the analyzed temperature to climatology. If the TOPS predicted temperature T_k^p does not change from day to day, then the analyzed temperature T_k^a will decay toward climatology T_k^c, with ν_k representing the percent anomaly reduction per analysis cycle (i.e., per day). The number of days, D, required to reduce the anomaly to 10% of the starting value is thus

$$D = \left[\frac{ln(0.1)}{ln(1 - \nu_k)}\right] = \left[\frac{ln(0.1)}{ln(\beta_k)}\right] . \tag{6-4}$$

Equation (2-2) reduces to

$$1 = (1 + \lambda_k^p)\beta_k . \tag{6-5}$$

From (6-5) and (2-5), β_k can be expressed in terms of σ_k^c and σ_k^p. Thus,

$$\beta_k = \frac{(\sigma_k^c)^2}{(\sigma_k^c)^2 + (\sigma_k^p)^2} . \tag{6-6}$$

From (6-6) and (2-19), the mean-square error of the resulting analysis can be written as

$$(\sigma_k^a)^2 = \frac{(\sigma_k^c \sigma_k^p)^2}{(\sigma_k^c)^2 + (\sigma_k^p)^2} . \qquad (6\text{-}7)$$

Now, with no data inputs, the mean-square analysis error will reach a steady state $(\sigma_k^s)^2$ at gridpoint k. But, from (2-11), recognizing that $(\sigma_k^a)^2_{INITIAL}$ will be given by $(\sigma_k^s)^2$, we have

$$(\sigma_k^p)^2 = (\sigma_k^s)^2 + G_k^2 . \qquad (6\text{-}8)$$

Substitution of (6-8) into (6-7) and replacement of $(\sigma_k^a)^2$ in (6-7) with $(\sigma_k^s)^2$, yields a quadratic equation for $(\sigma_k^s)^2$, whose solution is

$$(\sigma_k^s)^2 = G_k [\frac{1}{4} G_k^2 + (\sigma_k^c)^2]^{0.5} - \frac{1}{2} G_k^2 . \qquad (6\text{-}9)$$

Certain limiting values for the TOPS error growth parameter are of interest in (6-9). If G_k equals 0, then $(\sigma_k^s)^2$ also equals zero. Thus, if the prediction model is *perfect* (i.e., has zero error growth rate), then the analysis error tends toward zero in the asymptotic steady state. If G_k equals σ_k^c, then $(\sigma_k^s)^2$ equals approximately $0.62(\sigma_k^c)^2$. Thus, even with this large error growth rate, the prediction model is able to contribute some useful information to the analysis; without its input, the analysis error would tend toward $(\sigma_k^c)^2$ in the steady state. If G_k equals $3\sigma_k^c$, then $(\sigma_k^s)^2$ equals approximately $0.91(\sigma_k^c)^2$, and the TOPS predictions contribute little to reducing the analysis error. Finally, as G_k approaches infinity, $(\sigma_k^s)^2$ approaches $(\sigma_k^c)^2$.

From (6-3), (6-6), (6-8), and (6-9), the anomaly reduction factor ν_k can be expressed as

$$\nu_k = \frac{\frac{1}{2} G_k^2 + G_k [\frac{1}{4} G_k^2 + (\sigma_k^c)^2]^{0.5}}{(\sigma_k^c)^2 + \frac{1}{2} G_k^2 + G_k [\frac{1}{4} G_k^2 + (\sigma_k^c)^2]^{0.5}} . \qquad (6\text{-}10)$$

Limiting values for G_k are again of interest. If G_k equals 0, then ν_k also equals 0 and (6-2) reduces to

$$T_k^a = T_k^p . \qquad (6\text{-}11)$$

Thus, in the case of a perfect model, the analysis will simply carry the model prediction forward in time with no restoration toward climatology. If G_k equals σ_k^c, then ν_k equals approximately 0.62 and (6-2) reduces to

$$T_k^a = T_k^p - 0.62 (T_k^p - T_k^c) . \qquad (6\text{-}12)$$

In this case, a rather strong restoring force toward climatology is imposed on each analysis cycle. As G_k approaches infinity, ν_k approaches 1 and (6-2) reduces to

$$T_k^a = T_k^c . \qquad (6\text{-}13)$$

Thus, if the prediction model has no skill at all ($G_k \rightarrow \infty$), the analysis simply reproduces climatology in the long-term absence of data, *regardless* of what changes the prediction model forecasts. Table 6-1 shows ν_k and D as a function of G_k for σ_k^c equal to 1.0°C.

From (2-19) and (6-3), the steady-state mean-square error of the analysis can be expressed as

$$(\sigma_k^s)^2 = (\sigma_k^c)^2 (1 - \beta_k) = (\sigma_k^c)^2 \nu_k . \qquad (6\text{-}14)$$

Table 6-1. Anomaly reduction factor ν_k and number of days D for the analyzed thermal anomaly to be reduced to 10% of initial value at data-void gridpoint as a function of TOPS error growth rate G_k. Assumes one analysis cycle per day and σ_k^c equal to 1.0°C.

G_k(°C)	ν_k	D (days)
0.00	0.00	∞
0.03	0.03	76.7
0.04	0.04	57.6
0.05	0.05	46.0
0.06	0.06	38.4
0.07	0.07	33.0
0.08	0.08	28.8
0.09	0.09	25.6
0.10	0.09	23.0
0.15	0.14	15.4
0.20	0.18	11.5
0.25	0.22	9.2
0.30	0.26	7.7
0.35	0.29	6.6
0.40	0.33	5.8
0.60	0.45	3.9
1.00	0.62	2.4
2.00	0.83	1.3
3.00	0.91	1.0
∞	1.00	0.0

Thus, the values of ν_k in Table 6-1 can also be interpreted as the ratio of steady-state mean-square analysis error to the mean-square error of climatology for various TOPS error growth rates G_k.

6.2 Isolated Observation at a Gridpoint

Here we investigate the response of the analysis system to an isolated SST observation following an extended period for which no data were available. In this situation, equation (2-1) becomes

$$T_k^a = T_k^c + \alpha_k (T_k^o - T_k^c) + \beta_k (T_k^p - T_k^c), \quad (6\text{-}15)$$

which can be written

$$T_k^a = \alpha_k T_k^o + \beta_k T_k^p + \gamma_k T_k^c \quad (6\text{-}16)$$

where γ_k is the weight applied to climatology, given by

$$\gamma_k = 1 - \alpha_k - \beta_k . \quad (6\text{-}17)$$

Furthermore, equation (2-2) reduces to

$$\eta_{ki} = (1 + \lambda_k^o)\alpha_k + \eta_{ki}\beta_k , \quad (6\text{-}18a)$$

and

$$1 = \eta_{ki}\alpha_k + (1 + \lambda_k^p)\beta_k , \quad (6\text{-}18b)$$

where we have made use of the fact that $\eta_{ik} = \eta_{ki}$. Simultaneous solution of (6-18a) and (6-18b) yields

$$\alpha_k = \frac{\eta_{ki}\lambda_k}{(1 - \eta_{ki}^2) + \lambda_k^p + \lambda_k^p\lambda_k^o + \lambda_k^o} \quad (6\text{-}19)$$

and

$$\beta_k = \frac{(1 - \eta_{ki}) + \lambda_k^o}{(1 - \eta_{ki}^2) + \lambda_k^p + \lambda_k^p\lambda_k^o + \lambda_k^o} . \quad (6\text{-}20)$$

6.2.1 Initial Response of the Analysis to an Observation Made Precisely at the Gridpoint at Analysis Time

If the isolated observation is made precisely at the gridpoint at analysis time, then $\eta_{ki} = 1$ and (6-19) and (6-20) reduce to

$$\alpha_k = \frac{\lambda_k^p}{\lambda_k^p + \lambda_k^p\lambda_k^o + \lambda_k^o} \quad (6\text{-}21)$$

and

$$\beta_k = \frac{\lambda_k^o}{\lambda_k^p + \lambda_k^p\lambda_k^o + \lambda_k^o} , \quad (6\text{-}22)$$

Four cases are of interest.

Case 1: Perfect prediction, imperfect observation. As demonstrated in the previous section, a perfect prediction model (i.e., one for which $G_k = 0$) yields $\sigma_k^a = \sigma_k^s = 0$, thus implying $\lambda_k^p = 0$. From (6-15), (6-21), and (6-22) with $\lambda_k^p = 0$ and $\lambda_k^o \neq 0$, we find

$$T_k^a = T_k^p . \quad (6\text{-}23)$$

Thus, the data are completely ignored and the analysis reproduces the TOPS prediction exactly.

Case 2: Imperfect prediction, perfect observation. In this case, the observation is assumed perfect; and thus, $\lambda_k^o = 0$. Note that this case could occur only if *both* the instrumental *and* the subgrid-scale errors of the observation were zero. From (6-15), (6-21), and (6-22) with $\lambda_k^o = 0$ and $\lambda_k^p \neq 0$, we find

$$T_k^a = T_k^o . \quad (6\text{-}24)$$

Thus, the TOPS prediction is ignored completely, and the analysis system reproduces the observation exactly.

Case 3: Perfect prediction, perfect observation. In this case, $\lambda_k^p = \lambda_k^o = 0$. Also, since the prediction and the observation are both "perfect," they must equal each other. Thus, $T_k^p = T_k^o$. From (6-15) with $T_k^p = T_k^o$, and (6-18a) or (6-18b) with $\lambda_k^p = \lambda_k^o = 0$ and $\eta_{ki} = 1$, we find

$$T_k^a = T_k^o = T_k^p . \quad (6\text{-}25)$$

Thus, the analysis exactly reproduces the observation and the TOPS prediction, which is equal to the observation.

Case 4: Imperfect prediction, imperfect observation. This case is, of course, the general "real-world" case for which λ_k^p and λ_k^o both differ from zero. Equations (2-4) through (2-9), (2-12), (6-8), (6-9), (6-21), (6-22), and (6-17), along with the instrumental error parameters of Table 3-1, yield the weight applied to the isolated observation α_k, the weight applied to the TOPS prediction β_k, and the weight applied to climatology γ_k as a function of G_k, λ_k^n, σ_k^c, and the observational type (an additional parameter, M, the number of MCSST reports averaged to form a super ob, is also a factor in determining the weight for the

MCSST data). Tables 6-2 and 6-3 show α_k, β_k, and γ_k for the different observational types as a function of G_k and λ_k^n for $\sigma_k^c = 1.0$ °C.

As illustrated by the data presented in Tables 6-2 and 6-3, the weight given to the TOPS predictions β_k falls off rapidly with increasing TOPS error growth rate G_k. The analysis effectively "loses confidence" in the TOPS predictions and relies increasingly on the data and climatology (i.e., α_k and γ_k increase) as the TOPS error growth rate increases. Increasing γ_k^n implies less accurate data as a result of higher subgrid-scale noise contamination in the observations. Thus, for a fixed error growth rate, the weight given to TOPS and the weight given to climatology γ_k increase with increasing noise-to-signal ratio λ^n as the weights given to the various types of observations α_k decrease. For M (the number of MCSST reports averaged to form a super ob) equal to 1, the highest weight is assigned to bathy reports, the next highest weight to MCSST reports, and the least weight to ship reports, reflecting the relative instrumental accuracies of these data. As λ_k^n increases for a fixed value of G_k, the weights assigned to the observations tend to become more even as the subgrid-scale noise obscures the differences in instrumental accuracy. For $M = 50$ and $M = 100$, the MCSST super obs become the dominant observation. Note that increasing M from 50 to 100 has only a small impact on the weight assigned to the MCSST super ob.

6.2.2 Time-varying Response of the Analysis to an Observation Made Precisely at the Gridpoint at Analysis Time

In this section we investigate the time-varying response of the analysis system to an isolated bathy SST observation made precisely at the analysis gridpoint. Using equations (2-3), (2-4), (2-5), (2-7), (2-11), (2-12), (2-19), (6-9), (6-14), (6-17), (6-19), and (6-20), we produce time series of σ_k^a, α_k, β_k, and γ_k, which illustrate this response.

Figure 6-1(a) shows time series of the weight assigned to the observation α_k, the weight assigned to TOPS β_k, and the weight assigned to climatology γ_k for $\lambda_k^n = 0.5$, $\sigma_k^c = 1$°C, and $G_k = 0.2$°C. On Days 1

Table 6-2 Weights given to isolated observation at a gridpoint α_k, TOPS prediction β_k, and climatology γ_k as a function of TOPS error growth rate G_k and observational type, assuming $\lambda_k^n = 0.5$ and $\sigma_k^c = 1.0$°C. M is the number of MCSST reports averaged at a gridpoint to form a super ob.

G_k(°C)	α, β, γ for Ship Ob	α, β, γ for Bathy Ob	α, β, γ for MCSST Super Ob
0.10	0.02 0.89 0.09	0.16 0.76 0.08	0.05 0.86 0.09 (M = 1) 0.52 0.43 0.05 (M = 50) 0.59 0.37 0.04 (M = 100)
0.20	0.03 0.79 0.18	0.25 0.61 0.14	0.09 0.75 0.16 (M = 1) 0.67 0.27 0.06 (M = 50) 0.72 0.23 0.05 (M = 100)
1.00	0.10 0.34 0.56	0.53 0.18 0.29	0.25 0.29 0.46 (M = 1) 0.87 0.05 0.08 (M = 50) 0.90 0.04 0.06 (M = 100)
3.00	0.14 0.08 0.78	0.63 0.03 0.34	0.32 0.06 0.62 (M = 1) 0.91 0.01 0.08 (M = 50) 0.93 0.01 0.06 (M = 100)

Table 6-3. Same as Table 6-2, but for $\lambda_k^n = 1.5$.

G_k(°C)	α, β, γ for Ship Ob	α, β, γ for Bathy Ob	α, β, γ for MCSST Super Ob
0.10	0.01 0.89 0.10	0.06 0.85 0.09	0.03 0.87 0.10 (M = 1) 0.47 0.47 0.06 (M = 50) 0.55 0.40 0.05 (M = 100)
0.20	0.03 0.80 0.18	0.11 0.73 0.16	0.06 0.77 0.17 (M = 1) 0.62 0.31 0.07 (M = 50) 0.69 0.25 0.06 (M = 100)
1.00	0.08 0.35 0.57	0.29 0.27 0.44	0.18 0.31 0.51 (M = 1) 0.85 0.06 0.09 (M = 50) 0.89 0.04 0.07 (M = 100)
3.00	0.12 0.08 0.80	0.37 0.06 0.57	0.24 0.07 0.69 (M = 1) 0.89 0.01 0.10 (M = 50) 0.92 0.01 0.07 (M = 100)

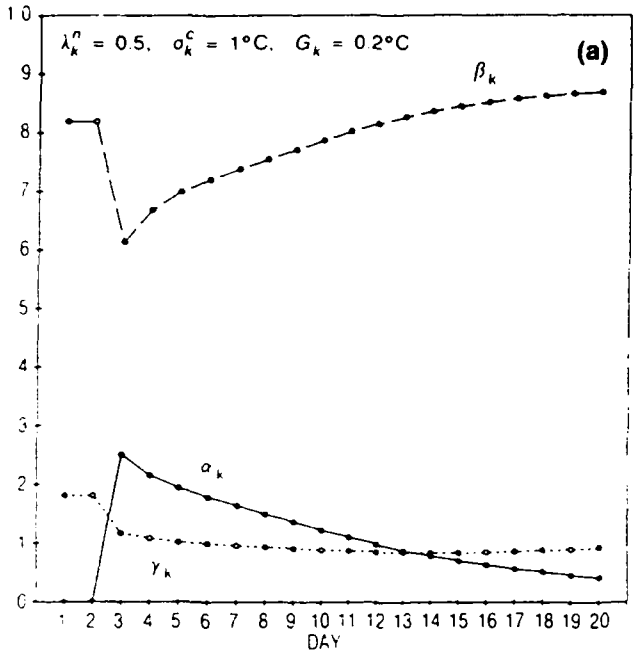

Figure 6-1(a). Time series of the weight given to TOPS β_k, the weight given to the observation α_k, and the weight given to climatology γ_k for a single bathy SST observation. The observation was made precisely at the analysis gridpoint at Day 3 following an extended period for which no data were available. The noise-to-signal ratio λ_k^n, the RMS variation of the resolvable thermal anomalies about climatology σ_k^c, and the TOPS error growth rate G_k are taken to be 0.5, 1°C, and 0.2°C, respectively.

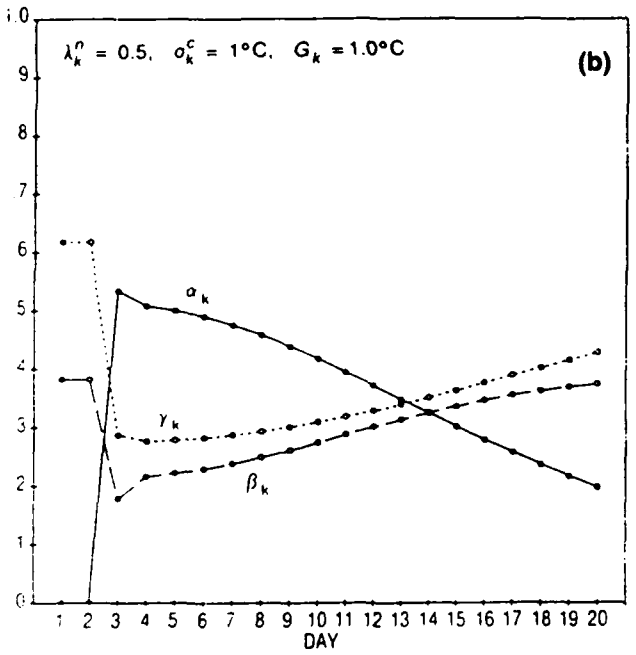

Figure 6-1(b). Same as Figure 6-1(a), but for G_k = 1.0°C.

and 2, β_k and γ_k exhibit their data-void steady-state values associated with the prescribed value of G_k. The bathy observation is made on Day 3 and the weights immediately adjust in response to it. The magnitude of β_k drops abruptly in response to the observation, and then increases asymptotically back to its data-void steady-state value. This change reflects the *updating* of the TOPS prediction with the information supplied by the observation at Day 3, and the *carrying of this information forward in time* by the TOPS model. The magnitude of α_k decays monotonically to zero from its initial non-zero value at Day 3, reflecting the loss of information as the observation "ages." The weight given to climatology γ_k takes on a minimum at about Day 13 before returning asymptotically to its data-void steady-state value.

Figure 6-1(b) shows time series of α_k, β_k, and γ_k for the same scenario as Figure 6-1(a), except with G_k = 1.0°C. In this case, the analysis has much less "confidence" in the TOPS prediction because of the larger TOPS error growth rate. As a result, compared to the previous case, more weight is given to both the observation and climatology, and less weight is given to TOPS. Also, the weights return to their data-void steady-state values more quickly in this situation than before, as TOPS is less effective in carrying information forward in time.

6.3 Two Observations Near a Gridpoint

In this section we investigate the initial response of the analysis system to two bathy SST observations made precisely at analysis time following an extended period for which no data were available. To simplify the geometry, the observations are distributed in a straight line that passes through the gridpoint location. By varying the location of the observations along this line, we can illustrate the dependence of the assigned weights and the resulting analysis error on data distribution.

The weights given to the two observations, α_1 and α_2, and the weight given to TOPS β are determined from (2-2), (2-3), (2-4), (2-5), (2-7), (2-11), (2-12), and (6-9). The analysis error σ_k^a is determined from (2-19). In the cases that follow, we assume λ_k^n = 0.5, G_k = 0.2°C, σ_k^c = 1°C, and A_k = 1/1500 km. Figure 6-2 shows the results for five different distributions of data.

Figure 6-2(a) shows results for both observations collocated with the gridpoint. Both observations receive the same weight, but this weight is about 20% less than the weight given to a *single* bathy observation made at the gridpoint for the combination of parameters considered (see Table 6-2). This weight reduction is because there is *redundancy* in the two observations as a result of their collocation. Nevertheless, the error achieved for this case is the minimum of all the test cases as the observations are the most highly correlated with the gridpoint.

Figure 6-2(b) shows results for observation 1 displaced 300 km to the left of the gridpoint and observation 2 displaced 300 km to the right of the gridpoint. Because of the symmetrical distribution of the data, both observations receive the same weight. The error is higher than that of Case 2(a) because the observations are less correlated with (i.e., farther away from) the gridpoint than before.

Figure 6-2(c) shows results for observation 1 displaced 600 km to the left of the gridpoint and observation 2 displaced 300 km to the right of the gridpoint. Because it is more highly correlated with (i.e., closer to) the gridpoint than observation 2, observation 1 receives a higher weight. The analysis error for Case 2(c) is higher than that of Case 2(b) because observation 1 is farther away from the gridpoint in Case 2(c).

Figure 6-2(d) shows results for both observations displaced 300 km to the left of the gridpoint. Both observations receive the same weight, but this weight is lower and the analysis error is higher than in Case 2(b). These results reflect the higher redundancy of the observations caused by their collocation.

Finally, Figure 6-2(e) shows results for observations 1 and 2 displaced 600 and 300 km to the left of the gridpoint, respectively. Note that the weight given to observation 1 is approximately 30% less than in Case 2(c), since observation 2 falls between observation 1 and the gridpoint. Note also that the analysis error is higher in Case 2(e) than in Case 2(c) because both observations are on the same side of the gridpoint (and thus more redundant) in Case 2(e).

In general, the results of Figure 6-2 illustrate the *nonlinear* aspect of the OI data assimilation technique. That is, the weights assigned to observations depend strongly on the distribution of the observations relative to each other, as well as relative to the analysis gridpoint.

7.0 Horizontal Analysis Grids

OTIS can function on the standard FNOC 63 × 63 northern hemisphere and southern hemisphere polar stereographic grids. These grids cover the entire northern and southern hemispheres with mesh lengths varying from about 380 km in high latitudes to about 200 km in the tropics. In addition, it can run on relocatable 63 × 63 or 125 × 125 regional polar stereographic grids of arbitrary location, extent, and orientation. Finally, OTIS can function on a relocatable rectangular latitude/longitude grid covering an arbitrary domain with dimensions up to 80 × 180. Grid spacings for regional applications of OTIS are typically 20-40 km.

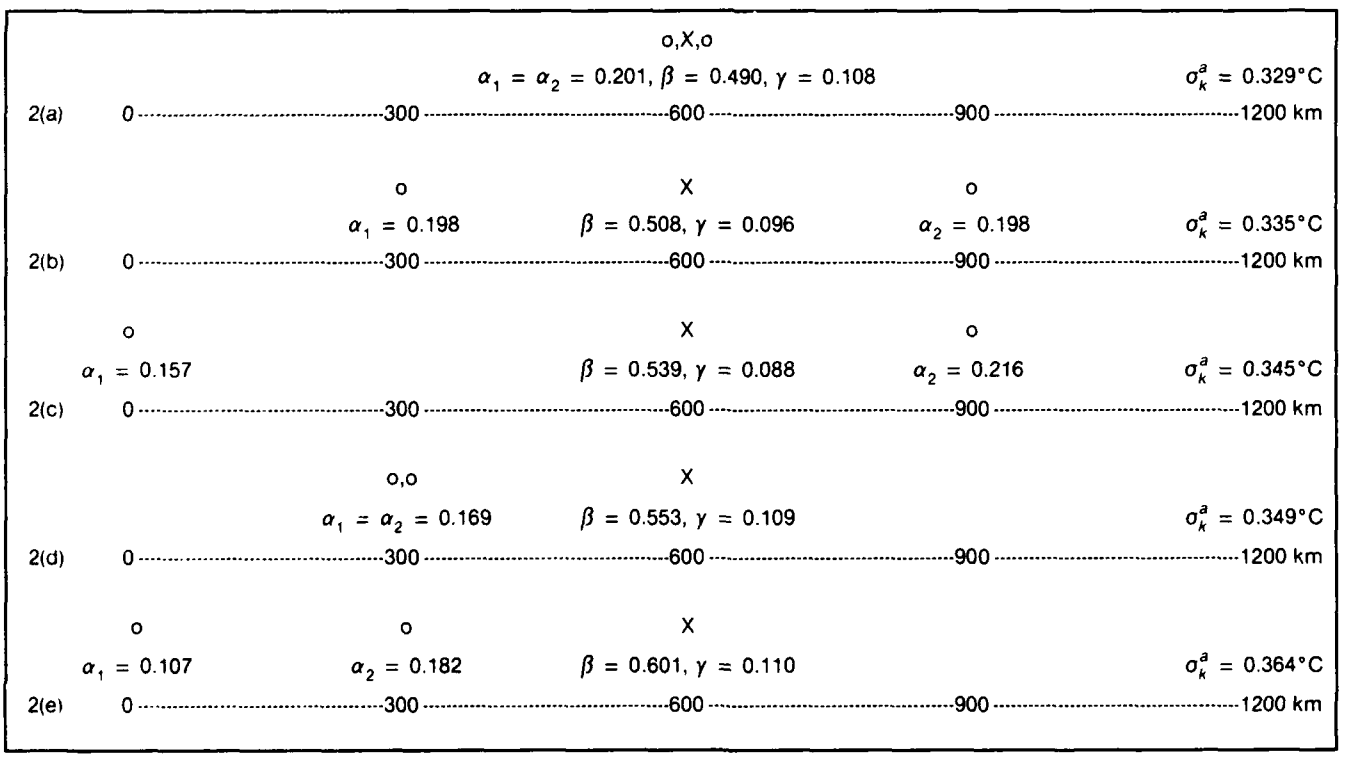

Figure 6-2. Analysis error σ_k^a and weights given to two bathy SST observations α_1 and α_2, TOPS β, and climatology γ, for observations made at analysis time following an extended period of no data. The observational locations are indicated by the o's and the gridpoint location is indicated by the X. The scale along the bottom of each figure shows distance in kilometers. All results assume $\lambda_k^n = 0.5$, $G_k = 0.2°C$, $\sigma_k^c = 1°C$, and $A_k = 1/1500$ km.

8.0 Supporting Climatologies

OTIS can utilize either the FNOC hemispheric climatology (Mendenhall et al., 1980) or the Generalized Digital Environmental Model climatology (GDEM; Davis et al., 1986) to supply T_k^c. The FNOC climatology is defined by month on the standard FNOC northern hemisphere and southern hemisphere 63 × 63 polar stereographic grids. The GDEM climatology is defined by season on a 0.5° latitude/longitude grid encompassing the north Atlantic, the north Pacific and the Mediterranean. Both climatologies exist in disk-resident form on the FNOC computer system and are automatically interpolated in time and space to the appropriate analysis time and grid by OTIS.

9.0 Ocean Feature Models

To account for the subsurface thermal structure of ocean fronts and eddies, ocean feature models can be automatically embedded in the OTIS first-guess field at known front and eddy locations obtained from satellite imagery. These models are basically canonical three-dimensional ocean front and eddy structures based on historical cruise data and dynamical insight (see Spall, 1986; Bennett et al., 1989). This feature-model embedding process produces subsurface thermal structures in the vicinity of fronts and eddies that are dynamically consistent with surface currents and substantially more accurate than climatology, even in the absence of any subsurface data. In conjunction with the ocean feature models, the data decorrelation option in OTIS is utilized to confine the influence of observations to the water masses in which they are made. Thus, data are not "smeared" laterally across fronts and the boundaries of eddies, resulting in a sharper depiction of these features.

10.0 Example Output

In this section we present output from the global-scale implementation of OTIS. The analysis shown here is generated on the FNOC 63 × 63 northern and southern hemispheric polar stereographic grids. The graphics are produced by interpolating the fields to a 2.5° spherical grid and then contouring. Because of the coarse resolution, mesoscale fronts and eddies are not represented in these products.

Figures 10-1 and 10-2 show SST and SST anomaly (analyzed temperature minus climatology) valid on 4 February 1988. The contour interval for SST is 1°C. The contour interval for SST anomaly is 0.5°C; negative anomalies are shown with a solid line, and positive anomalies are shown with a dashed line. As indicated by Figure 10-2, prominent large-scale anomalies are present throughout the world's oceans. Of note are (1) the two cold anomalies in the midlatitude north Pacific larger than -2.5°C and centered at 42°N, 172°E and 36°N, 153°E; (2) the warm anomaly in the western tropical north Pacific larger than 2.0°C and centered at 25°N, 152°E; and (3) the warm anomaly in the midlatitude south Atlantic larger than 3.0° and centered at 32°S, 7°W.

Figures 10-3 and 10-4 show temperature and temperature anomaly at the 200-m depth from the 4 February 1988 analysis. As before, the contour interval for temperature is 1°C, the contour interval for temperature anomaly is 0.5°C, negative anomaly contours are displayed with a solid line, and positive anomaly contours are displayed with a dashed line. From Figure 10-4, large-scale anomalies at the 200-m depth are prominent in the Pacific. Of particular note are (1) the cold anomaly in the western tropical Pacific larger than -3.5°C and centered at 7°N, 155°E; (2) the two warm anomalies in the eastern tropical Pacific larger than 1.5°C and centered at 20°N, 139°W and 17°N, 155°W; and (3) the warm anomaly in the tropical south Pacific larger than 3.0°C and centered at 12°S, 142°W.

11.0 Validation

As increasingly sophisticated ocean thermal models become available for operational use, it is imperative to have the means of rigorously and objectively establishing their relative skill. This validation requires consistent comparison of the models against the same independent, accurate ocean thermal data. A system to carry out this process automatically and routinely using bathy data is in place at FNOC (SASC, 1984, 1985; Clancy et al., 1986; Clancy et al., in press). This system is used for validating OTIS and other ocean thermal models at FNOC and provides a detailed and complete archive of model performance. Results of these validations are published in the FNOC *Quarterly Model Performance Summaries*, and are used to ensure that new models or techniques implemented operationally are indeed more skillful than the old ones they replace.

The thermal fields from OTIS, TOPS, and other models are interpolated once per day to the locations of all bathy observations received at FNOC during the previous 24 hours, but not yet assimilated into the models (making the observations independent of the models). Each bathy observation is then vertically interpolated to a standard grid between the surface and 300 m, and spurious observations are automatically discarded by a bathy error detection algorithm (see SASC, 1985).

A full suite of error statistics for temperatures at depths of 0, 12.5, 25, 50, 75, 100, 150, 200, and 300 m are calculated from the remaining bathy observations in various fixed geographical regions (e.g., Eastern Pacific, Western Atlantic, etc.). These statistics include

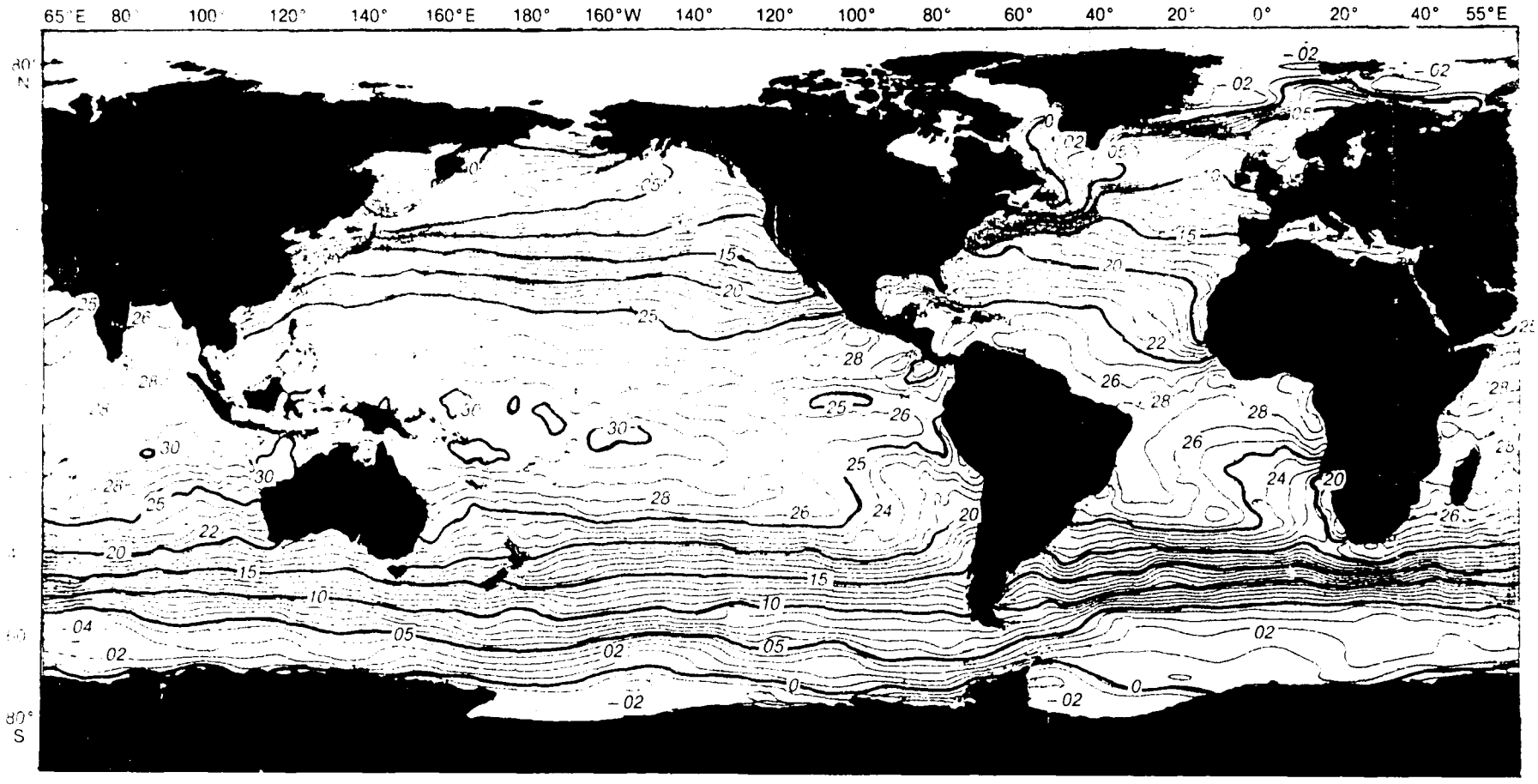

Figure 10-1. Global-scale SST from OTIS valid on 4 February 1988. The contour interval is 1°C.

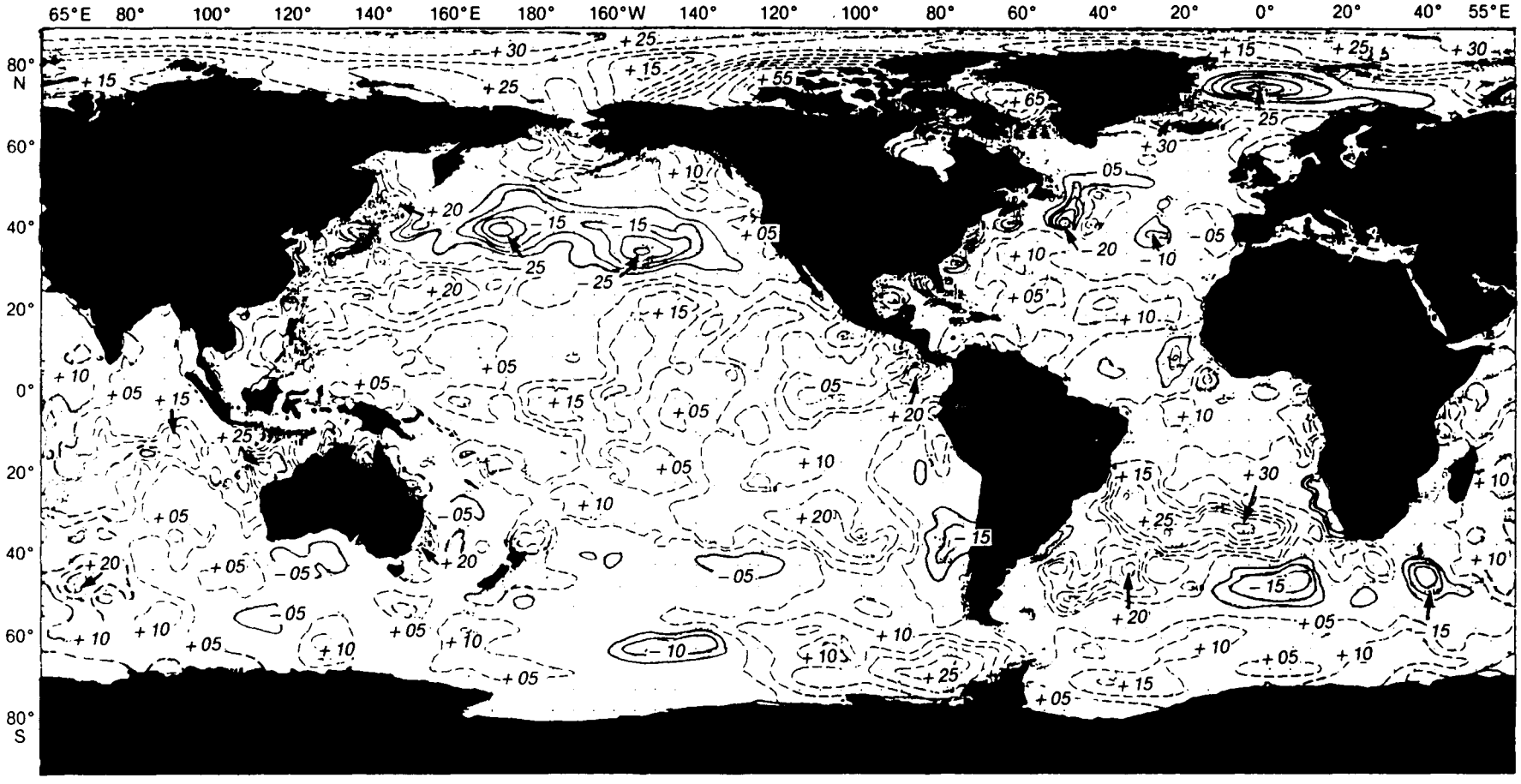

Figure 10–2. Global-scale SST anomaly (analyzed temperature minus climatology) from OTIS valid on 4 February 1988. The contour interval is 0.5°C and decimal points are suppressed in the labeling. Thus, for example, a contour label of 25 implies 2.5°C. Negative contours are shown with a solid line and positive contours are shown with a dashed line.

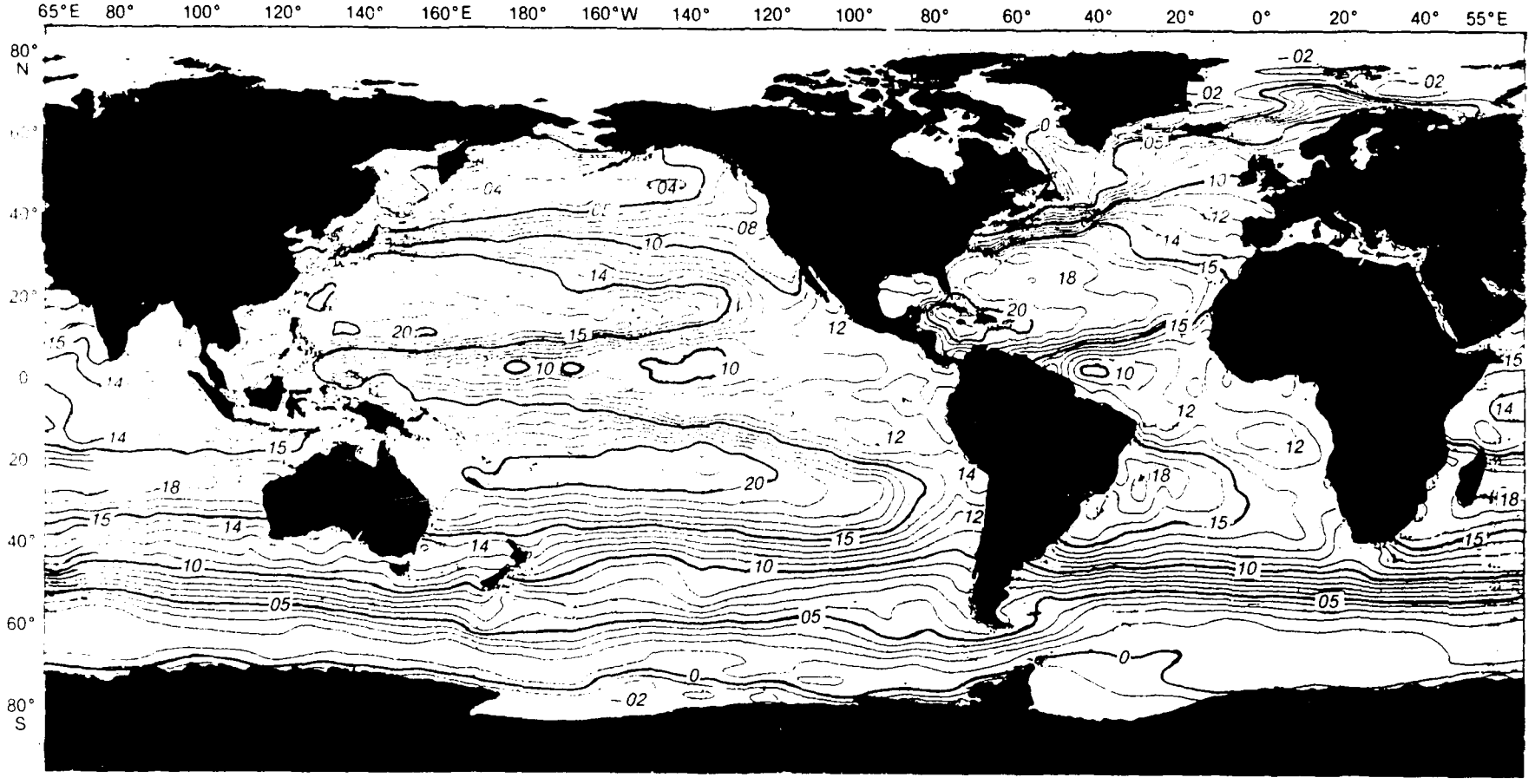

Figure 10-3. Global-scale temperature at 200 m depth from OTIS valid on 4 February 1988. The contour interval is 1°C.

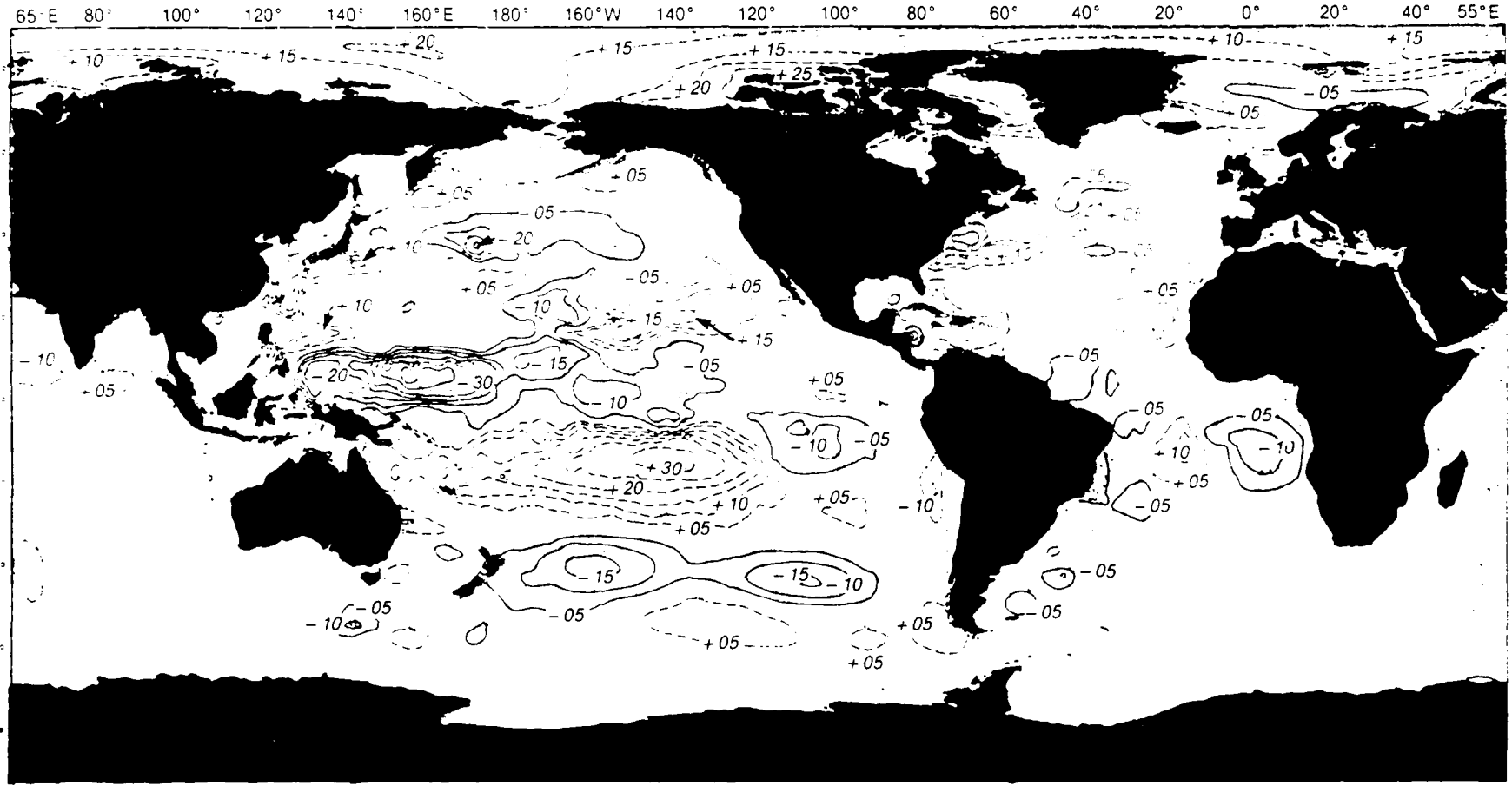

Figure 10-4. Global-scale temperature anomaly at 200 m depth (analyzed temperature minus climatology) from OTIS valid on 4 February 1988. The contour interval is 0.5°C and the decimal points are suppressed in the labeling. Thus, for example, a contour label of 25 implies 2.5°C. Negative contours are shown with a solid line and positive contours are shown with a dashed line.

the root-mean-square (RMS) error, the mean error, and the systematic RMS error.

The RMS error is the square root of the mean of the squared differences between the observed temperatures at various depths and the OTIS analyzed temperatures. Because the temperature differences are squared, errors of opposite sign do not cancel in this statistic, and it thus supplies information on the model's skill at predicting the *pattern* of the thermal field. Generally, RMS error tends to be contaminated by observational noise, due partly to instrumental errors that are not screened out by the error-checking algorithms and partly to subgrid-scale errors associated with thermal features of spatial extent too small to be resolved by the model grid. If the observational noise is large, then it can obscure the true difference in the performance of models.

The mean error is simply the average of the predicted minus observed temperatures at various depths. It gives an indication of *bias* in the predicted thermal fields over the entire verification domain, but tends to average out model errors characterized by spatially varying signs (e.g., too warm in part of the domain but too cold in another). Thus, unlike the RMS error, the mean error supplies no information on how well the model predicts the pattern of the thermal field. Observational error (which has a zero mean) is suppressed in the mean error statistic.

The systematic RMS error is defined as the square root of the mean of the squared differences between the observed temperatures and the least-squares regression line through the scatter of predicted versus observed temperatures at various depths. Like the RMS error, this statistic provides information on the model's ability to represent the pattern of the thermal field. Unlike RMS error, however, it tends to suppress the effects of observational noise in the verification data; it thus allows for a more valid intercomparison of model performance than the RMS error (see Willmott, 1981, 1982).

These statistics are calculated from running 30-day and 90-day histories of the predicted minus observed temperatures, and are output in graphical form. The resulting plots show profiles of the error statistics from the surface down to the 300-m depth. Figure 11-1 is an example that shows RMS, mean, and systematic RMS error for Northern Hemisphere (NHEM) OTIS and climatology in the eastern North Pacific (30-70°N, 120-175°W) for the month of January 1988 from comparison against 406 independent bathy observations. OTIS clearly exhibits substantial improvements over climatology in all three sets of statistics.

12.0 Summary and Future Developments

OTIS is an ocean thermal analysis system designed for operational use at FNOC. It is based on the Optimum Interpolation data assimilation technique and functions in an analysis-forecast-analysis data assimilation cycle with TOPS. OTIS provides a rigorous framework for combining real-time data (e.g., ship, buoy, bathy, and satellite observations), predictions from an ocean forecast model (e.g., TOPS, OCEANS, etc.), and ocean thermal climatology (e.g., GDEM) to produce a statistically optimum representation of ocean thermal structure. OTIS outputs the thermal field on a vertically stretched grid with either 17 fixed levels in the upper 400 m (shallow analysis mode) or 34 fixed levels in the upper 5000 m (deep analysis mode), and can function on hemispheric or relocatable regional grids that employ either polar stereographic or spherical projections. Figure 12-1 illustrates the central role OTIS plays in linking various data bases and models to produce a comprehensive ocean thermal analysis and prediction system.

OTIS Version 1 became operational at FNOC on the NHEM and SHEM 63 × 63 polar stereographic grids in July 1988 (see Clancy et al., in press). It was upgraded to function on the FNOC NHEM and SHEM 125 × 125 polar stereographic grids in July 1989, thereby doubling the spatial resolution of FNOC's global-scale representation of ocean thermal structure. OTIS Version 2, designed only for regional-scale eddy-resolving applications and relying heavily on use of ocean feature models, became operational at FNOC for the Gulf Stream region in June 1989. OTIS Version 3, which employs a more sophisticated use of ocean feature models and supporting data bases, is currently being implemented to run on the CYBER 205 and, eventually, the Large Scale Computer (LSC) at FNOC.

A future development will involve the use of satellite altimetry data to construct synthetic bathy profiles for use by OTIS. This data may prove to be an important source of thermal information below the 400-m depth. In addition, the ocean feature models and supporting data bases used by OTIS to add definition to the subsurface thermal field associated with fronts and eddies will be improved and extended to all regions of Navy interest. Finally, the statistical parameters required by OTIS will be refined as experience with the system grows.

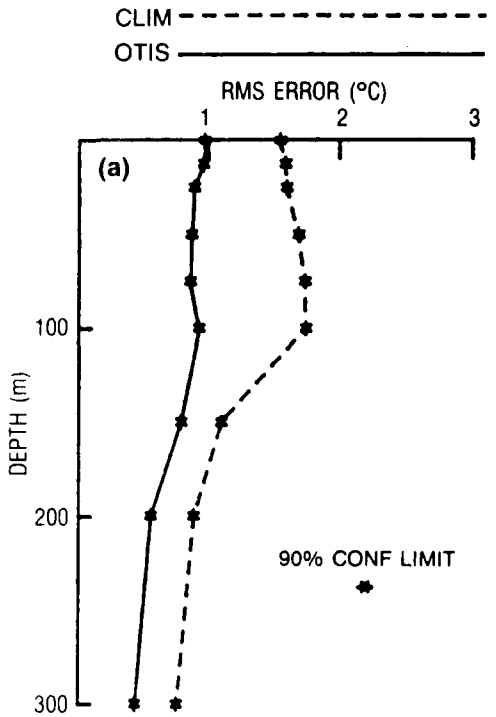

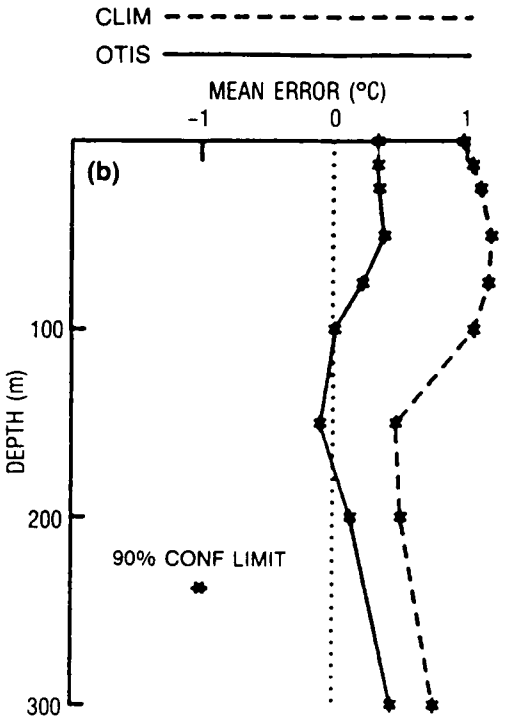

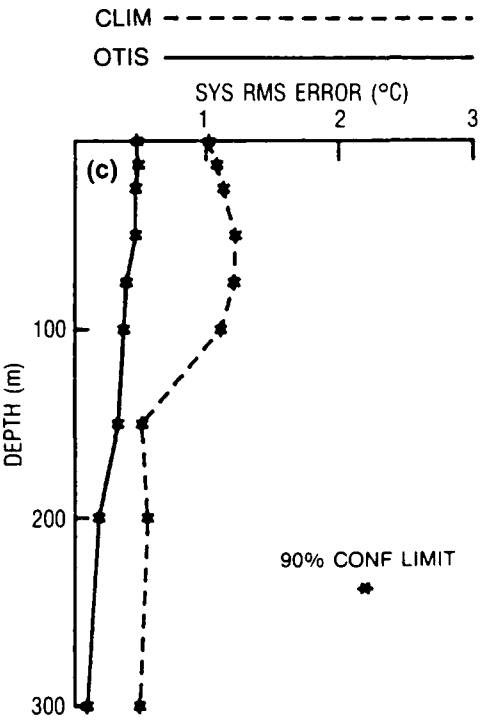

Figure II-1. (a) RMS, (b) mean, and (c) systematic RMS temperature errors for NHEM OTIS (solid line) and climatology (dashed line) for the eastern North Pacific (30-70°N, 120-175°W) during the month of January 1988. The statistics are based on comparison against 406 independent bathy observations and the error bars indicate approximate 90% confidence limits.

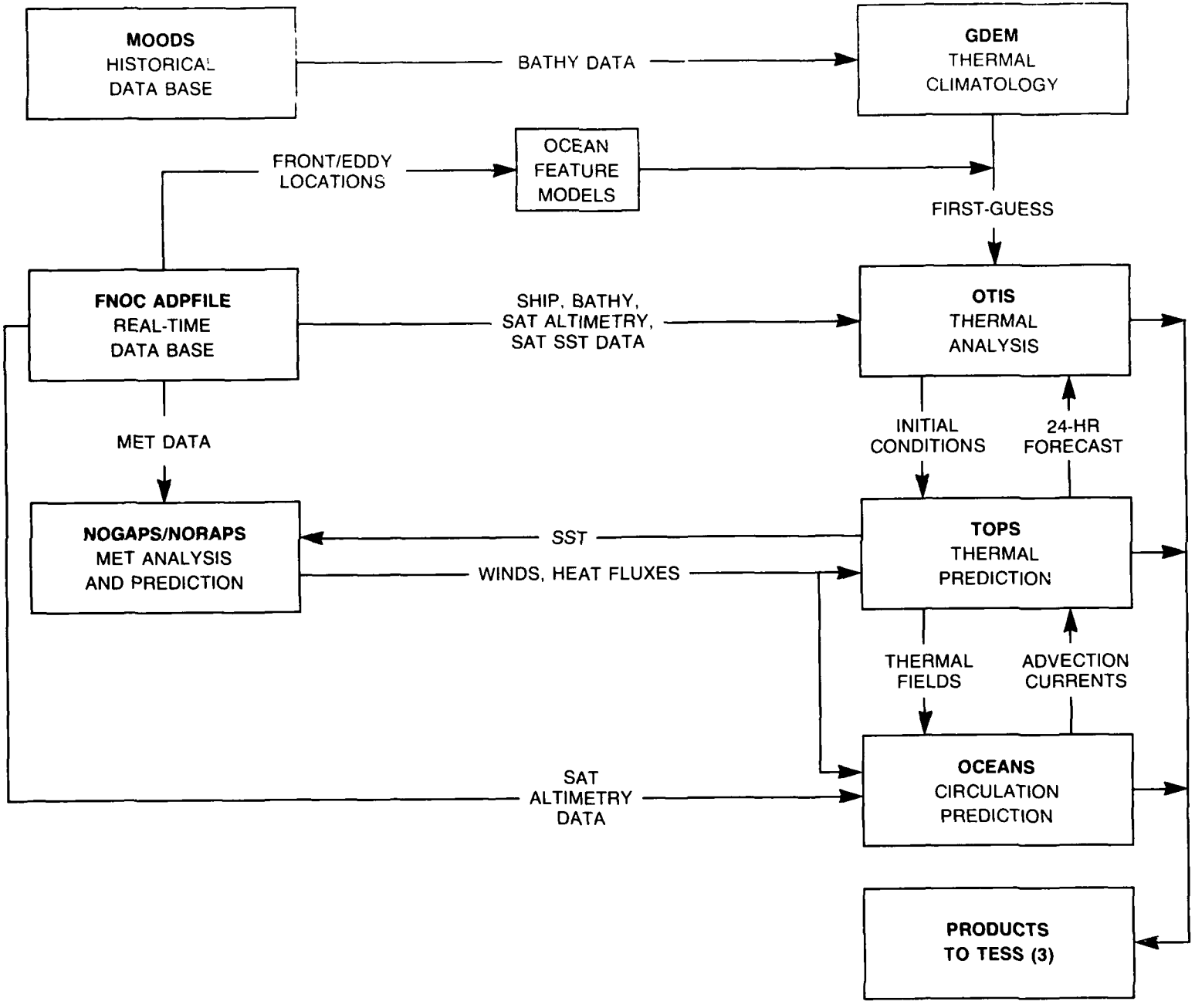

Figure 12-1. Schematic diagram illustrating the relationship of OTIS to various data bases and models.

13.0 References

Alaka, M. A. and R. C. Elvander (1972). Optimum Interpolation from Observations of Mixed Quality. *Monthly Weather Review* 100: 612-624.

Beasley, M. E. (1987). *Changes in the California Current System Observed Off Northern California During July-August 1986.* Naval Postgraduate School, Monterey, CA 93943, Masters Thesis, NPS-68-88-002.

Bennett, T. J, M. R. Carnes, P. Phoebus, and L. M. Riedlinger (1989). *Feature Modeling: Incorporation of a Front and Eddy Map into Optimum Interpolation-Based Thermal Analyses.* Naval Ocean Research and Development Activity, Stennis Space Center, MS 39529. NORDA Report 242, 24 pp.

Bengtsson, L. and N. Gustafsson (1972). Assimilation of Non-synoptic Observations. *Tellus* 24: 383-399.

Bergman, K. (1978). Role of Observational Errors in Optimum Interpolation Analysis. *Bulletin of the American Meteorological Society* 59: 1603-1611.

Bernstein, R. L. and W. B. White (1981). Stationary and Traveling Mesoscale Perturbations in the Kuroshio Extension Current. *Journal of Physical Oceanography* 11: 692-704.

Bretherton, F. P., R. E. Davis, and C. B. Fandry (1976). A Technique for Objective Analysis and Design of Oceanographic Experiments Applied to MODE-73. *Deep-Sea Research* 23: 559-582.

Carter, E. F. and A. R. Robinson (1981). Time Series of Synoptic Maps of the Western North Atlantic: A Space-Time Objective Analysis of POLYMODE XBT's. *Reports in Meteorology and Oceanography*, Number 15, Division of Applied Sciences, Harvard University.

Carter, E. F. and A. R. Robinson (1987). Analysis Models for the Estimation of Oceanic Fields. *Journal of Atmospheric and Oceanic Technology* 4: 49-74.

Carter, E. F., A. R. Robinson, and P. S. Bogden (1988). The Kinematics, Statistics and Maps of the Temperature and Velocity Fields in the POLYMODE Synoptic Dynamics Experiment. (Manuscript in preparation, Division of Applied Sciences, Harvard University).

Carton, J. A. (1987). How Predictable are the Geostrophic Currents in the Recirculation Zone of the North Atlantic? *Journal of Physical Oceanography* 17: 751-762.

Clancy, R. M. (1983). The Effect of Observational Error Correlations on Objective Analysis of Ocean Thermal Structure. *Deep-Sea Research* 30: 985-1002.

Clancy, R. M. and P. J. Martin (1981). Synoptic Forecasting of the Oceanic Mixed Layer Using the Navy's Operational Environmental Data Base: Present Capabilities and Future Applications. *Bulletin of the American Meteorological Society* 62: 770-784.

Clancy, R. M. and K. D. Pollak (1983). A Real-Time Synoptic Ocean Thermal Analysis/Forecast System. *Progress in Oceanography* 12: 383-424.

Clancy, R. M., K. D. Pollak, and J. M. Harding (1986). Validation of Ocean Thermal Models at Fleet Numerical Oceanography Center. *Proceedings, Marine Data Systems International Symposium,* New Orleans, April 30-May 2, Marine Technology Society, 2000 Florida Ave. NW, Suite 500, Washington, DC 20009, 332-337.

Clancy, R. M., P. A. Phoebus, and K. D. Pollak (in press). An Operational Global-Scale Ocean Thermal Analysis System. *Journal of Atmospheric and Oceanic Technology.*

Cummings, J. A. (1986). Water Mass Climatology in the NW Atlantic with Application to Optimal Field Estimation. *Transactions of the American Geophysical Union* 67: 1038.

Davis, T. M., K. A. Countryman, and M. J. Carron (1986). Tailored Acoustic Products Utilizing the NAVOCEANO GDEM (A Generalized Digital Environmental Model). Paper presented at the *36th Naval Symposium on Underwater Acoustics,* March 1986, San Diego, CA.

Dimego, G., P. Phoebus, and J. McDonald (1985). Data Processing and Quality Control for Optimum Interpolation Analyses at the National Meteorological Center. National Meteorological Center, Washington, D.C. 20233, NMC Office Note 306.

Dorman, C. E. and J. F. T. Saur (1978). Temperature Anomalies Between San Francisco and Honolulu, 1966-1974, Gridded by an Objective Analysis. *Journal of Physical Oceanography* 8: 247-257.

Earle, M. D. (1985). *Statistical Comparisons of Ship and Buoy Marine Observations.* MEC Systems Corporation, 10629 Crestwood Drive, Manassas, VA 22110, Technical Report MEC-85-8.

FNOC (1986). *Fleet Numerical Oceanography Center Products Manual, Volume II: Meteorological and Oceanographic Models.* Commander Naval Oceanography Command, Stennis Space Center, MS 39529.

Freeland, H. J. and W. J. Gould (1976). Objective Analysis of Mesoscale Ocean Circulation Features. *Deep-Sea Research* 23: 915-923.

Gandin, L. S. (1965). Objective Analysis of Meteorological Fields. *Israel Program for Scientific Translations,* Jerusalem, 242 pp.

Grillaki-Steiert, D. and V. Amoroso (1988). *Analysis Systems for the Mesoscale Thermal Variability in the Greenland-Iceland-Norwegian Sea.* SACLANT Undersea Research Centre, La Spezia, Italy, Memorandum Report SM-212.

Haney, R. L. (1974). A Numerical Study of the Response of an Idealized Ocean to Large-Scale Surface Heat and Momentum Flux. *Journal of Physical Oceanography* 4: 145-167.

Hansen, D. V. and A. Herman (1986). Simple Drifting Buoy Statistics on Surface Currents and SST in the Tropical Pacific: Sampling Implications for the TOGA and WOCE Programs. *Proceedings of the Workshop on Drifting Buoy Data Quality Control,* 17-18 July 1986, National Data Buoy Center, Stennis Space Center, MS 39529, 106-141.

Hawkins, J. D., J. M. Harding, J. R. Chase, R. M. Clancy, and B. L. Samuels (1986). *The Impact of Satellite Infrared Sea Surface Temperatures on FNOC Ocean Thermal Analyses.* Naval Ocean Research and Development Activity, Stennis Space Center, MS 39529, NORDA Report 142.

Hodur, R. M. (1982). Description and Evaluation of NORAPS: The Navy Operational Regional Atmospheric Prediction System. *Monthly Weather Review* 110: 1591-1602.

Hua, L. B., J. C. McWilliams, and W. B. Owens (1986). An Objective Analysis of the POLYMODE Local Dynamics Experiment. Part II: Streamfunction and Potential Vorticity Fields During the Intensive Period. *Journal of Physical Oceanography* 16: 506-522.

Hurlburt, H. E. (1984). The Potential for Ocean Prediction and the Role of Altimeter Data. *Marine Geodesy* 8: 17-66.

Innis, G. E. (1983). *Progress in Implementing the Optimum Thermal Interpolation System (OTIS) at FNOC.* Science Applications International Corporation, 1200 Prospect St., P.O. Box 2351, La Jolla, CA 92038, Technical Report SAI-085-83-429-LJ.

Innis, G. E. (1985). *Further Development and Implementation of the Optimum Thermal Interpolation System (OTIS) at FNOC.* Science Applications International Corporation, 1200 Prospect St., P.O. Box 2351, La Jolla, CA 92038, Technical Report SAIC-85-1635.

Innis, G. E. and B. R. Mendenhall (1986). *Enhancements to the Optimum Thermal Interpolation System.* Science Applications International Corporation, 205 Montecito Ave., Monterey, CA 93940, Technical Report SAIC-1-425-06-481.

Martin, P. J., J. M. Harding, J. D. Hawkins, and R. M. Clancy (1985). The FNOC TOPS/TEOTS Ocean Thermal Forecast/Analysis System. *Naval Research Reviews* 37: 3-7.

McLain, D. R., P. D. Stevens, and R. A. Bauer (1986). Real-Time Reporting of Ocean Temperature and Salinity Profiles. *Proceedings of the Marine Data Systems International Symposium,* 30 April-2 May, New Orleans, Marine Technology Society, 2000 Florida Ave. NW, Suite 500, Washington, DC 20009.

McWilliams, J. C. (1976). Maps from the Mid-Ocean Dynamics Experiment: Part I. Geostrophic Streamfunction. *Journal of Physical Oceanography* 6: 810-827.

McWilliams, J. C., W. B. Owens and L. B. Hua (1986). An Objective Analysis of the POLYMODE Local Dynamics Experiment. Part I: General Formalism and Statistical Model Selection. *Journal of Physical Oceanography* 16: 483-504.

Mellor, G. L. and T. Yamada (1974). A Hierarchy of Turbulence Closure Models for Planetary Boundary Layers. *Journal of the Atmospheric Sciences* 31: 1791-1806.

Mellor, G. L. and P. A. Durbin (1975). The Structure and Dynamics of the Ocean Surface Mixed-Layer. *Journal of Physical Oceanography* 5: 718-725.

Mendenhall, B. R. and M. J. Cuming (1980). *SHIPTRK: A System for Recognizing and Correcting Position Errors in Marine Synoptic Weather and Bathythermograph Reports.* Meteorology International Incorporated, 2600 Garden Road, Suite 145, Monterey, CA 93940, Technical Report M-245-03.

Mendenhall, B. R., M. J. Cuming and M. M. Holl (1980). *Update of Monthly Northern Hemisphere Climatologies of Upper Ocean Thermal-Structure Parameters.* Meteorology International Incorporated, 2600 Garden Road, Suite 145, Monterey, CA 93940, Final Report, MII Project No. M-249.

Murray, J. J. (1987). *An Analysis of Horizontal Temperature Gradients and Heat Content in the Mixed Layer and of the Surface Forcing During PATCHEX.* Naval Postgraduate School, Monterey, CA 93943, Masters Thesis, NPS-68-ST.

Phoebus, P. A. (1988). *Improvements to the Data Selection Algorithm in the Optimum Thermal Interpolation System (OTIS).* Naval Ocean Research and Development Activity, Stennis Space Center, MS 39529, NORDA Report 239, 18 pp.

Phoebus, P. A. (1989). *Quality Control Algorithms for Ocean Temperature Data.* Naval Ocean Research and Development Activity, Stennis Space Center, MS 39529, NORDA Report (in preparation).

Pollard, R. T. and R. C. Millard (1970). Comparison Between Observed and Simulated Wind-Generated Inertial Oscillations. *Deep-Sea Research* 17: 813-821.

Robinson, A. R. (1983). Description and Prediction of Oceanic Fields: Data Assimilation and Optimal Estimation. *Proceedings of the Study Conference on Large-Scale Oceanographic Experiments in the World Climate Research Programme,* CCO/SCOR-JSC/WCRP, Tokyo.

Robinson, A. R. and W. G. Leslie (1985). Estimation and Prediction of Oceanic Eddy Fields. *Progress in Oceanography* 14: 485-510.

Robinson, A. R. (1986). Data Assimilation, Mesoscale Dynamics and Dynamical Forecasting. *Proceedings of the NATO Advanced Studies Institute on Ocean Models,* J. J. O'Brien (ed.).

Robinson, A. R. and L. J. Walstad (1986). The Harvard Open Ocean Model: Calibration and Application to Dynamical Process, Forecasting, and Data

Assimilation Studies. *Journal of Applied Numerical Mathematics* 3(1-2): 89-131.

Robinson, A. R., J. A. Carton, N. Pinardi, and C. N. K. Mooers (1986). Dynamical Forecasting and Dynamical Interpolation: An Experiment in the California Current. *Journal of Physical Oceanography* 16: 1561-1579.

Robinson, A. R., A. Hecht, N. Pinardi, J. Bishop, W. G. Leslie, Z. Rosentroub, A. J. Mariano, and S. Brenner (1987). Small Synoptic/Mesoscale Eddies and Energetic Variability of the Eastern Levantine Basin. *Nature* 327: 131.

Roden, G. I. (1977). Oceanic Subarctic Fronts of the Central Pacific: Structure of and Response to Atmospheric Forcing. *Journal of Physical Oceanography* 7: 761-778.

Roden, G. I. and D. F. Paskausky (1978). Estimation of Rates of Frontogenesis and Frontolysis in the North Pacific Ocean Using Satellite and Surface Meteorological Data from January 1977. *Journal of Geophysical Research* 83: 4545-4550.

Roemmich, D. (1983). Optimal Estimation of Hydrographic Station Data and Derived Fields. *Journal of Physical Oceanography* 13: 1544-1549.

Rosmond, T. E. (1981). NOGAPS: Navy Operational Global Atmospheric Prediction System. Preprint Volume, *Fifth Conference on Numerical Weather Prediction,* Monterey, published by the American Meteorological Society, Boston, pp. 74-79.

SAIC (1988a). *Users Manual for the Optimum Thermal Interpolation System (OTIS Version 1).* Science Applications International Corporation, 205 Montecito Avenue, Monterey, CA 93940.

SAIC (1988b). *Program Maintenance Manual for the Optimum Thermal Interpolation System (OTIS Version 1).* Science Applications International Corporation, 205 Montecito Avenue, Monterey, CA 93940.

SAIC (1988c). *Computer Operation Manual for the Optimum Thermal Interpolation System (OTIS Version 1).* Science Applications International Corporation, 205 Montecito Avenue, Monterey, CA 93940.

SASC (1984). *Ocean Thermal Product Validation Programs: Functional Description/Users Manual.* Systems and Applied Sciences Corporation, 570 Casanova Ave., Monterey, CA 93940, Technical Report 6602.

SASC (1985). *Users Manual: Vertical Temperature Profile Validation System, A Part of the Ocean Thermal Product Validation Programs.* Systems and Applied Sciences Corporation, 570 Casanova Ave., Monterey, CA 93940, Technical Report 6607.

Spall, M. (1986). An Operational Forecast Excercise in the Gulf Stream Meander and Ring Formation Region. Department of Earth and Planetary Science, Harvard University, Cambridge, MA 02138, unpublished manuscript.

Strong, A. E. and E. P. McClain (1985). Improved Ocean Surface Temperatures from Space-Comparison with Drifting Buoys. *Bulletin of the American Meteorological Society* 65: 138-142.

STX (1987). *Upgrades to OTIS.* ST Systems Corporation (STX), 1900 Garden Road, Suite 130, Monterey, CA 93940, Technical Report STI 6617.

White, W. B. (1977). Secular Variability in the Baroclinic Structure of the Interior North Pacific from 1950-1970. *Journal of Marine Research* 4: 587-607.

White, W. B. and R. L. Bernstein (1979). Design of an Oceanographic Network in the Midlatitude North Pacific. *Journal of Physical Oceanography* 9: 592-606.

Willmott, C. J. (1981). On the Validation of Models. *Physical Geography* 2: 184-194.

Willmott, C. J. (1982). Some Comments on the Evaluation of Model Performance. *Bulletin of the American Meteorological Society* 63: 1309-1313.

Appendix

Basic Theory of Optimum Interpolation

Here we derive equation (2-2) of Section 2, which is the fundamental equation of OI as implemented in OTIS. Let f_i represent the ith estimate of a field to be mapped to a discrete grid. Estimates are obtained from observations and the predictions from a numerical model, and we can write

$$f_i = F_i + E_i \tag{A-1}$$

where F_i is the "true" representative value of the field on the scale resolved by the grid and E_i is the error in the ith estimate. If f_i is an observation, then E_i is the observational error due to the combined effects of both instrumental and aliasing (i.e., subgrid-scale) errors. If f_i is the predicted field from a numerical model functioning on the same grid as the target analysis, then E_i is simply the grid-scale error in the model prediction.

The deviation of the mapped field from a first-guess field is represented as a weighted combination of the estimated departures from the first guess. This representation is subject to error, and we can thus write

$$F_k' = \sum_{i=1}^{N+1} f_i' p_i + I_k \tag{A-2}$$

where F_k' is the true representative value at gridpoint k, p_k is the weight given to the ith estimate, $N + 1$ is the number of estimates assimilated at the gridpoint, and I_k is the analysis error at the gridpoint. The primes denote departure from the first-guess field, which is assumed to be the long-term climatology and thus an unbiased estimator.

From equations (A-1) and (A-2), the mean-square analysis error at gridpoint k over an ensemble of analysis realizations is given by

$$\overline{I_k^2} = \overline{[\sum_{i=1}^{N+1} (F_i' + E_i) p_i - F_k']^2} \tag{A-3}$$

which can be expanded to

$$\overline{I_k^2} = \sum_{i=1}^{N+1} \sum_{j=1}^{N+1} p_i p_j (\overline{F_i' F_j'} + \delta_{ij} \overline{E_i' E_j'}) - 2 \sum_{i=1}^{N+1} p_i \overline{F_i' F_k'} + \overline{F_k' F_k'} \tag{A-4}$$

where the overbar denotes an ensemble mean over many analysis realizations, δ_{ij} is the delta function ($\delta_{ij} = 1$ for $i = j$; $\delta_{1j} = 0$ for $i \neq j$), and we have made the usual assumptions that the correlations between the errors of the estimates and the true deviations from the first-guess field of climatology (i.e., $\overline{E_i' F_j'}$), and the correlations between the errors of the estimates (i.e., $\overline{E_i' E_j'}$ for $i \neq j$) are zero (see Bergman, 1978). Dividing (A-4) by the variance of F' *(i.e.,* $\overline{F_k' F_k'}$) yields

$$\Psi = \frac{\overline{I_k^2}}{\overline{F_k' F_k'}} = \sum_{i=1}^{N+1} \sum_{j=1}^{N+1} p_i p_j (\eta_{ij} + \delta_{ij} \lambda_i) - 2 \sum_{i=1}^{N+1} p_i \eta_{ki} + 1 \qquad \text{(A-5)}$$

where Ψ is the normalized mean-square analysis error,

$$\eta_{ij} = \frac{\overline{F_i' F_j'}}{\overline{F_k' F_k'}} \qquad \text{(A-6)}$$

and

$$\lambda_i = \frac{\overline{E_i' E_i'}}{\overline{F_k' F_k'}} \, . \qquad \text{(A-7)}$$

The quantity η_{ij} is the space-time autocorrelation function between locations i and j in sampling space for the resolvable signal F', and λ_i is the noise-to-signal ratio.

To obtain the optimum values of the weights p_i applied to the estimates of the target field f_i', the normalized mean-square analysis error Ψ is minimized by setting

$$\frac{\partial \Psi}{\partial p_i} = 0 \, . \qquad \text{(A-8)}$$

From (A-5), this yields

$$\sum_{j=1}^{N+1} (\eta_{ij} + \delta_{ij} \lambda_i) p_j = \eta_{ki} \; (i = 1, 2, 3 \ldots N + 1). \qquad \text{(A-9)}$$

Now, in the context of OTIS, the first N estimates are observations (i.e., ship, bathy, and satellite data) and the $N + 1$th estimate is a prediction from the TOPS model. Using the subscript k to denote the kth analysis gridpoint and defining the weights applied to the observations as α_{kj}, the weight applied to TOPS as β_k, the noise-to-signal ratio for the observations as λ_i^o, and the noise-to-signal ratio for TOPS as λ_k^p, equation (A-9) reduces to

$$\sum_{j=1}^{N} (\eta_{ij} + \delta_{ij} \lambda_i^o) \alpha_{kj} + (\eta_{ik} + \delta_{ik} \lambda_k^p) \beta_k = \eta_{ki}$$

$$\text{for } i = 1, 2 \ldots, N, (N + 1) = k \qquad \text{(A-10)}$$

which is precisely equation (2-2) of Section 2.

Distribution List

Admiralty Research Establishment
Ocean Science Division
Southwell
Portland, Dorset DT5 2JS England
Attn: Mr. G. Kirby

Atlantic Oceanographic and
Meteorological Laboratory
4301 Rickenbacker Causeway
Virginia Key FL 33149
Attn: Dr. G. Maul

Applied Physics Laboratory
Johns Hopkins University
John Hopkins Road
Laurel MD 20707
Attn: Director
Dr. J. Apel
Dr. J. Calman

Applied Physics Laboratory
University of Washington
1013 NE 40th St.
Seattle WA 98105
Attn: Director

Applied Research Laboratory
Pennsylvania State University
P.O. Box 30
State College PA 16801
Attn: Director

Applied Research Laboratory
University of Texas at Austin
P.O. Box 8029
Austin TX 78713-8029
Attn: Director

Assistant Secretary of the Navy
Research, Engineering & Systems
Washington DC 20350-1000

Cal Space
5360 Bothe Ave.
San Diego CA 92122
Attn: Dr. R. Bernstein

Chief of Naval Operations
Washington DC 20350-2000
Attn: OP-02
OP-71
OP-987

Chief of Naval Operations
Oceanographer of the Navy
Washington DC 20392-1800
Attn: OP-09, Mr. R. Winokur
OP-096
OP-96B

CIMAS
4600 Rickenbacker Causeway
Virginia Key FL 33149
Attn: Director

David W. Taylor Naval Research Center
Bethesda MD 20084-5000
Attn: Commander

Defense Mapping Agency
Systems Center
12100 Sunset Hill Rd. #200
Reston VA 22090-3207
Attn: Director
Code SGWN

Department of Fisheries & Oceans
Ocean Circulation Division
P.O. Box 1006
Dartmouth, Nova Scotia
B2Y 4A2 Canada
Attn: Dr. F. Dobson

Department of Physical Oceanography
4600 Rickenbacker Causeway
Miami FL 33149
Attn: Dr. T. Lee

Department of the Navy
Director of Navy Laboratories
Crystal Plaza #5, Rm. 1062
Washington DC 20360

Fleet Antisub Warfare Tng Ctr-Atlantic
Naval Station
Norfolk VA 23511-6495

Fleet Numerical Oceanography Center
Monterey CA 93943-5105
Attn: Commanding Officer
Code 40
Code 40B, Mr. L. Clarke
Code 42, Dr. J. Cummings
Code 42, Mr. R. M. Clancy (10)
Code 42, Mr. K. Pollak (5)
Code 43, Mr. J. Cornelius
Code 70B, Ms. P. Chavasant

Florida State University
Dept. of Physical Oceanography
Meteorology Annex 435 PSA Bldg.
930 Wildwood
Tallahassee FL 32306-3041
Attn: Dr. B. Cushman-Rosin

GFDL
Princeton University
P.O. Box 308
Princeton NJ 08542
Attn: Ms. B. Samuels
Dr. S. Levitus

Harvard University
Division of Applied Sciences
28 Oxford St.
Cambridge MA 02138
Attn: Dr. A. Robinson

Institute for Naval Oceanography
Building 1103
Stennis Space Center MS 39429
Attn: CDR E. Johnson
Dr. J. Leese

Institute of Ocean Sciences
P.O. Box 6000
9860 W. Saanich Rd.
Sidney BC V8L 4B2 Canada
Attn: Dr. A. Bennet

International Ice Patrol
Avery Point
Groton CT 06340-6096
Attn: Commander

Jet Propulsion Laboratory
California Institute of Technology
M/S 169-236
Pasadena CA 91109
Attn: Dr. D. Halpern

JOI
Suite 800
1755 Massachusetts Ave., NW
Washington DC 20036
Attn: Mr. F. Eden

Martin-Marietta Data Systems
c/o FNOC
Monterey CA 93943
Attn: Dr. P. May
Mr. H. Hamilton
Mr. B. Mendenhall
Mr. M. Ignaszewski

Massachusetts Institute of
Oceanography
Dept. of Earth & Planetary Sciences
Cambridge MA 02139
Attn: Dr. G. Flierl

NASA-Goddard Space Flight Center
Greenbelt MD 20771
Attn: Code 671, Dr. D. Adamec
Code 671, Dr. M. Reinecker
Code 912, Dr. T. Busalacchi

NASA Headquarters
Washington DC 20233
Attn: Dr. E. Njoku

NASA-Jet Propulsion Laboratory
4800 Oak Grove Dr.
Pasadena CA 91109
Attn: Code 183-501, Mr. D. Hagan

National Environmental Satellite Serv.
World Weather Building
Washington DC 20233
Attn: Code S/RE13, Dr. P. Deleonibus

National Data Buoy Center
Stennis Space Center MS 39529
Attn: Dr. G. Hamilton

National Geodetic Survey
Rockville MD 20852
Attn: Dr. R. Cheney

National Marine Fisheries Serv.
PEG, Southwest Fisheries Center
P.O. Box 831
Monterey CA 93942
Attn: Dr. D. McLain

National Meteorological Center
World Weather Building
Washington DC 20233
Attn: W/NMC2, Dr. G. DiMego
W/NMC2, Dr. J. Thiebaux
W/NMC4, Dr. C. Dey
W/NMC21, Dr. L. Breaker
W/NMC21, Mr. B. Gemmill
W/NMC52, Dr. A. Leetma

National Ocean Data Center
1825 Connecticut Ave., NW
Universal Bldg. South, Rm. 406
Washington DC 20235
Attn: G. Withee, Director

National Ocean Survey
Ocean Applications, Bldg. 4
Monterey CA 93943-5005
Attn: Dr. M. Holl

National Ocean Survey
Ocean Products Division,
WWB Rm. 201
5200 Auth Rd.
Camp Springs MD 20748
Attn: Mr. R. Barazotto
Dr. W. Campbell

National Space Science Data Center
4400 Forbes Blvd.
Lanham MD 20706
Attn: Ms. Mary Jones

National Weather Service
1325 East-West Hwy.
Silver Spring MD 20910
Attn: Wx1, Dr. R. McPherson

Naval Air Development Center
Warminster PA 18974-5000
Attn: Commander

Naval Air Systems Command HQ
Washington DC 20361-0001
Attn: Commander

Naval Civil Engineering Laboratory
Port Hueneme CA 93043
Attn: Commanding Officer

Naval Coastal Systems Center
Panama City FL 32407-5000
Attn: Commanding Officer

Naval Eastern Oceanography Center
McAdle Bldg. (U-117)
Naval Air Station
Norfolk VA 23511-5399

Naval Facilities Engineering
Command HQ
200 Stovall St.
Alexandria VA 22332-2300
Attn: Commander

Naval Oceanographic Office
Stennis Space Center MS 39522-5001
Attn: Commanding Officer
Code OS, Mr. L. Bernard
Code OS, Mr. M. Boston
Code OST, Mr. A. Johnson
Code OST, Mr. J. Rigney
Code OSTM, Dr. C. Horton
Code OSTM, Mr. R. Rhodes

Naval Oceanography Command
Stennis Space Center MS 39529-5000
Attn: Commander

Naval Oceanographic and Atmospheric
Research Laboratory
Stennis Space Center MS 39529-5004
Attn: Code 100
Code 105
Code 115
Code 125EX
Code 125L (10)
Code 125P
Code 200
Code 211, Dr. J. Caruthers
Code 222, Mr. G. Kerr
Code 223, Dr. D. King
Code 224, Mr. B. Northridge
Code 300
Code 311, Mr. K. Ferer
Code 320, Dr. J. McCaffrey
Code 321, Mr. J. Hawkins
Code 321, Mr. D. May
Code 321, Dr. J. Mitchell
Code 321, Mr. A. Pressman
Code 322, Dr. T. Bennett
Code 322, Dr. J. Harding
Code 322, Mr. P. Martin
Code 323, Dr. D. Blake
Code 323, Dr. G. Heburn
Code 323, Dr. H. Hurlburt
Code 323, Dr. D. Thompson
Code 331, Dr. J. Boyd
Code 331, Dr. Z. Hallock

Naval Oceanographic and Atmospheric
Research Laboratory
Monterey CA 93943-5006
Attn: Code 400
Code 430, Dr. E. Barker
Code 431, Dr. J. Goerss

Naval Oceanographic and Atmospheric
Research Laboratory
Liaison Office
Crystal Plaza #5, Rm. 802
Arlington VA 22202-5000
Attn: B. Farquhar

Naval Ocean Systems Center
San Diego CA 92152-5000
Attn: Commander

Naval Postgraduate School
Monterey CA 93943
Attn: Superintendent
Code 63, Dr. B. Renard
Code 63Hy, Prof. H. Haney
Code 68, Dr. C. Collins
Code 68Gd, Prof. B. Garwood

Naval Research Laboratory
Washington DC 20375
Attn: Commanding Officer

Naval Sea Systems Command HQ
Washington DC 20362-5101
Attn: Commander
Naval Surface Warfare Center
White Oak
10901 New Hampshire Ave.
Silver Spring MD 20904-5000
Attn: Commander
Library

Naval Surface Weapons Center
Dahlgren VA 22338-5000
Attn: Commander

Naval Surface Weapons Center Det
White Oak Laboratory
10901 New Hampshire Ave.
Silver Spring MD 20903-5000
Attn: Library

Naval Underwater Systems Center
Newport RI 02841-5047
Attn: Commanding Officer
Dr. Ding Lee

Naval Underwater Systems Center Det
New London Laboratory
New London CT 06320
Attn: Officer in Charge

Naval Western Oceanography Center
Box 113
Pearl Harbor HI 96860-5050
Attn: CDR P. Kelley

NCAR
P.O. Box 3000
Boulder CO 80307
Attn: Dr. R. Anthes

NESDIS
SRL (E/RA1)
Washington DC 20233
Attn: Dr. P. McClain
Dr. B. Pichel

NOAA/NOS International Affairs
U.S. Department of Commerce
14th & Constitution Ave., N.W.
Washington DC 20230
Attn: Ms. Muriel Cole
Dr. G. Flittner

Office of Naval Research
800 N. Quincy St.
Arlington VA 22217-5000
Attn: Code 10
Code 10D/10P, Dr. E. Silva
Code 112, E. Hartwig
Code 1122, Dr. D. Evans
Code 1122, Dr. T. Curtin
Code 1122, Dr. T. Kinder
Code 1122, Dr. T. Spence
Code 1122, Dr. A. Weinstein
Code 12
Code 120M, Mr. R. Peloquin

Office of Naval Research
ONR Branch Office
Box 39
FPO New York 09510-0700
Attn: Commanding Officer

Office of Naval Research
Coastal Sciences Program
Arlington VA 22217
Attn: Code 1122CS, Dr. A. Brandt

Office of Naval Technology
800 N. Quincy St.
Arlington VA 22217-5000
Attn: Code 20, Dr. P. Selwyn
Code 228, Dr. M. Briscoe
Code 234, C. Votaw

Oregon State University
College of Oceanography
Corvallis OR 97331
Attn: Prof. J. Allen

Pacific Marine Environmental
Research Laboratory
7600 Sand Point Way NE
Seattle WA 98115-0070
Attn: Dr. M. McPhaden

SAIC
205 Montecito Ave.
Monterey CA 93940
Attn: Dr. W. Denner

SAIC
4900 Water's Edge Dr., Suite 255
Raleigh NC 20706
Attn: Dr. V. Waddel

SAIC
10260 Campus Pt. Dr., Mail Stop 34
San Diego CA 92121
Attn: Dr. G. Innis

Sandia National Laboratories
Division 6334
Albuquerque NM 97185
Attn: Dr. S. Kuperman

Scripps Institution of Oceanography
La Jolla CA 92093
Attn: Dr. Cornuelle
Dr. D. Cutchin
Dr. S. Pazen
Dr. W. White

Scripps Institution of Oceanography
University of California
P.O. Box 6049
San Diego CA 92106

Space and Naval Warfare
Systems Command
2511 Jeff Davis Hwy.
Washington DC 20363-5100
Attn: Commander
Code PMW141, LCDR B. Cook
and CDR G. Trumbower

University of Colorado
Dept. of Aerospace Eng. Sciences
Campus Box 429
Boulder CO 80309-0429
Attn: Dr. G. Born

University of Miami
Center for Marine Studies
4600 Rickenbacker Causeway
Miami FL 33149-1098
Attn: Dr. Otis Brown

University of Oklahoma
Dept. of Meteorology
200 Felgar St.
Norman OK 93019
Attn: Dr. C. Duchon

University of Rhode Island
Graduate School of Oceanography
Kingston RI 02881
Attn: Dr. E. Carter

University of Rhode Island
Graduate School of Oceanography
Narragansett Bay Campus
Narragansett RI 02882
Attn: Dr. P. Cornillon

U.S. Naval Academy
Department of Oceanography
Annapolis MD 21402-5026
Attn: Chairman
Dr. A. Strong

U.S. Naval Observatory
34th and Massachusetts Ave., NW
Building 1
Washington DC 20392-1800
Attn: Mr. D. Montgomery

Woods Hole Oceanographic
Institution
P.O. Box 32
Woods Hole MA 02543
Attn: Dr. C. Dorman, Director
Dr. H. Bryden
Dr. J. Price

REPORT DOCUMENTATION PAGE

Form Approved
OMB No. 0704-0188

1. Agency Use Only *(Leave blank).*

2. Report Date. August 1989

3. Report Type and Dates Covered.

4. Title and Subtitle.

Technical Description of the Optimum Thermal Interpolation System, Version 1: A Model for Oceanographic Data Assimilation

5. Funding Numbers.

Program Element No. 63704N

Project No.

Task No.

Accession No. DN394457

6. Author(s).

*R. Michael Clancy, Patricia A. Phoebus, *Kenneth D. Pollak

7. Performing Organization Name(s) and Address(es).

Ocean Science Directorate
Naval Ocean Research and Development Activity
Stennis Space Center, Mississippi 39529-5004

8. Performing Organization Report Number.

NORDA Report 240

9. Sponsoring/Monitoring Agency Name(s) and Address(es).

Space and Naval Warfare Systems Command
Washington, DC

10. Sponsoring/Monitoring Agency Report Number.

11. Supplementary Notes.

*Ocean Models Division, Fleet Numerical Oceanography Center, Monterey, California 93943

12a. Distribution/Availability Statement.

Approved for public release; distribution is unlimited. Naval Ocean Research and Development Activity, Stennis Space Center, Mississippi 39529-5004.

12b. Distribution Code.

13. Abstract *(Maximum 200 words).*

The Optimum Thermal Interpolation System (OTIS) is an ocean thermal analysis product developed for real-time operational use at the Fleet Numerical Oceanography Center. OTIS is expected to become the centerpiece of the Navy's ocean thermal analysis ano prediction capabilities both ashore and afloat. It provides a rigorous framework for the synergistic combination of real-time data, climatology, and predictions from ocean mixed-layer and circulation models to produce the Navy's most accurate representation of ocean thermal structure on global and regional scales. OTIS is particularly well suited for utilization of remotely sensed data from satellites because of its ability to account for the relative accuracies of various types of data.

OTIS is based on the optimum interpolation (OI) data assimilation methodology. Basically, the OI technique maps observations distributed nonuniformly in space and time to a uniformly gridded synoptic representation, or analysis, of the target field. The analysis is constructed as a first-guess background field plus an anomaly relative to that field. The analyzed anomaly at a particular gridpoint is given by a weighted combination of observed and model-predicted anomalies, with the space-time autocorrelation function for the resolvable anomalies governing which observations contribute. The OI technique provides the optimum weights applied to each anomaly, such that the resulting analysis error will be minimized in a least-squares sense. The technique also provides an estimate of this error.

The basic inputs to OTIS are the statistics defining both the resolvable and subgrid-scale variability of the target field about the background field, the instrumental error characteristics of the measurement systems providing the observations, and the error characteristics of the forecast model that supplies the predictions. The end product is a statistically optimum gridded representation of the current ocean thermal structure, which may in turn be used to initialize prognostic thermodynamic and ocean circulation models, or to compute sound-speed profiles for input to ocean acoustic models.

14. Subject Terms.

satellite SST, remote sensing, thermodynamic ocean models, ocean thermal analysis, data assimilation, ocean thermal structure, optimum interpolation

15. Number of Pages. 37

16. Price Code.

17. Security Classification of Report.	18. Security Classification of This Page.	19. Security Classification of Abstract.	20. Limitation of Abstract.
Unclassified	Unclassified	Unclassified	None